

# Geophysical Methods for Stratigraphic Identification

September 2019

Judy Robinson  
Rob D Mackley  
Mark Rockhold  
Tim Johnson  
Piyoosh Jaysaval

## DISCLAIMER

This report was prepared as an account of work sponsored by an agency of the United States Government. Neither the United States Government nor any agency thereof, nor Battelle Memorial Institute, nor any of their employees, makes **any warranty, express or implied, or assumes any legal liability or responsibility for the accuracy, completeness, or usefulness of any information, apparatus, product, or process disclosed, or represents that its use would not infringe privately owned rights**. Reference herein to any specific commercial product, process, or service by trade name, trademark, manufacturer, or otherwise does not necessarily constitute or imply its endorsement, recommendation, or favoring by the United States Government or any agency thereof, or Battelle Memorial Institute. The views and opinions of authors expressed herein do not necessarily state or reflect those of the United States Government or any agency thereof.

PACIFIC NORTHWEST NATIONAL LABORATORY  
*operated by*  
BATTELLE  
*for the*  
UNITED STATES DEPARTMENT OF ENERGY  
*under Contract DE-AC05-76RL01830*

Printed in the United States of America

Available to DOE and DOE contractors from the  
Office of Scientific and Technical Information,  
P.O. Box 62, Oak Ridge, TN 37831-0062;  
ph: (865) 576-8401  
fax: (865) 576-5728  
email: [reports@adonis.osti.gov](mailto:reports@adonis.osti.gov)

Available to the public from the National Technical Information Service  
5301 Shawnee Rd., Alexandria, VA 22312  
ph: (800) 553-NTIS (6847)  
email: [orders@ntis.gov](mailto:orders@ntis.gov) <<https://www.ntis.gov/about>>  
Online ordering: <http://www.ntis.gov>

# **Geophysical Methods for Stratigraphic Identification**

September 2019

Judy Robinson  
Rob D Mackley  
Mark Rockhold  
Tim Johnson  
Piyooosh Jaysaval

Prepared for  
the U.S. Department of Energy  
under Contract DE-AC05-76RL01830

Pacific Northwest National Laboratory  
Richland, Washington 99354

## Summary

Although geophysics has been used for identifying subsurface fluid flow and contaminant spatial distributions at the Hanford Site and elsewhere, geophysics has not been generally used for identifying aquifer stratigraphy at environmentally relevant depths ( $> 70$  m). This is because the bulk geophysical measurements of aquifer sediments cannot be directly related to sediment properties due to competing effects (e.g., porosity, pore-fluid conductivity, grain-sizes), thereby restricting the ability of conventional geophysical tools from discriminating their variation. Electrical resistivity tomography (ERT) is a method that can overcome these limitations because time-lapsed imaging, demonstrating changes in these properties over time, can be obtained from field sensors that can be left in place.

This document reports on an innovative approach that combines field-scale tracer testing, ERT, and robust three-dimensional inversion of ERT data for identifying major stratigraphy. Specifically, the goal of the characterization work is to fully delineate (in 3D) a large-scale, high-permeability paleochannel that has been inferred to exist between the 200 West and 200 East Areas of the Hanford Site's Central Plateau. Because of its large-scale ( $> 3.2$  km<sup>2</sup>) and the high costs associated with drilling multiple boreholes at the Hanford Site, a cost-effective approach for paleochannel identification is needed. This paleochannel is of particular importance because it will have significant impact on flow and contaminant transport from 200 West to 200 East. Its high permeability can both accelerate contaminant transport and lower contaminant concentrations through spreading, which is information needed for making remedy decisions at Hanford.

To assess the viability of using ERT for paleochannel identification, a modeling approach that links a groundwater flow and transport model to ERT simulations was used. The groundwater model provided data that was converted to electrical conductivity, and the ERT simulation code, E4D, inverted the hypothetical electrical conductivity measurements to obtain subsurface images. Although the horizontal structure of the paleochannel could be imaged without a conductive tracer injection, the vertical resolution was limited. Once a conductive tracer injection was simulated, the results indicated that time-lapsed ERT monitoring could be used to delineate the large-scale paleochannel. However, additional site-specific information is needed to confirm its feasibility, such as a small-scale ERT campaign to obtain pertinent information relative to assessing ambient noise levels that can impact survey resolution at depth. Simulation results also indicated that a multi-year monitoring period is required since it will take a few years for the injected tracer to laterally migrate the hundreds of meters needed to fully characterize the paleochannel.

In addition to the ERT analysis, a thorough review of other geophysical methods for stratigraphic characterization is also presented in this report. This included a review of previous geophysical surveys executed at the Hanford Site. Field investigations using seismic, electromagnetic, and ERT methods have ranged from kilometer-scale mapping of supra-basalt sediments to meter-scale studies that are used to identify borehole and well locations within a plume footprint. Since some of these data sets have not yet been fully interpreted in 3D, it is recommended that these data be inverted using the state-of-the-art techniques provided in E4D.

## Acknowledgments

This document was prepared by the Deep Vadose Zone - Applied Field Research Initiative at Pacific Northwest National Laboratory. Funding for this work was provided by the U.S. Department of Energy (DOE) Richland Operations Office. The Pacific Northwest National Laboratory is operated by Battelle Memorial Institute for the DOE under Contract DE-AC05-76RL0183.

## Acronyms and Abbreviations

CCU	Cold Creek Unit
CRIM	Complex Refractive Index Model
EM	electromagnetics, active source
ERT	electrical resistivity tomography
FEM, FDEM	frequency-domain EM
GPR	ground penetrating radar
HEIS	Hanford Environmental Information System
IP	induced polarization
LERF	Liquid Effluent Retention Facility
MASW	multichannel analysis surface wave
NMR	nuclear magnetic resonance
NQAP	Nuclear Quality Assurance Program
OU	operable unit
P&T	pump-and-treat
PNNL	Pacific Northwest National Laboratory
RLM	Ringold lower mud
TEM, TDEM	time-domain EM
SASW	spectral analysis surface wave

# Contents

Summary .....	ii
Acknowledgments.....	iii
Acronyms and Abbreviations .....	iv
Contents .....	v
1.0 Introduction.....	1.1
1.1 Geophysical Surveys at Hanford .....	1.1
1.2 Report Organization.....	1.2
2.0 Hanford Site Geologic Description.....	2.1
3.0 Geophysical Methods Overview .....	3.1
3.1 Electrical Resistivity Tomography .....	3.2
3.1.1 Induced Polarization .....	3.2
3.2 Active Source Electromagnetics .....	3.3
3.3 Seismic.....	3.5
3.4 Ground Penetrating Radar.....	3.8
3.5 Magnetics.....	3.8
4.0 Previous Geophysical Work Done to Identify Preferential Flow Pathways at Hanford.....	4.1
4.1 Electromagnetics and Integration Investigations .....	4.1
4.2 Seismic and Integration Investigations .....	4.4
4.3 Electrical Resistivity Tomography .....	4.7
4.4 Ground Penetrating Radar.....	4.9
4.5 Conclusions / Recommendations of Previous Work.....	4.12
5.0 Evaluation of Electrical Resistivity Tomography .....	5.1
5.1 Site Description.....	5.2
5.2 Simulation Details.....	5.3
5.2.1 Flow and Transport.....	5.4
5.2.2 Petrophysical Transform.....	5.5
5.2.3 Electrical Resistivity Tomography .....	5.6
5.2.4 Other Modeling Considerations.....	5.7
5.3 Results.....	5.8
5.3.1 Flow and Transport.....	5.8
5.3.2 Electrical Resistivity Tomography .....	5.9
5.4 ERT Evaluation Conclusions .....	5.11
6.0 Summary and Recommendations .....	6.1
7.0 Quality Assurance.....	7.1
8.0 References.....	8.1
Appendix A Proposed Activities Needed to Support the ERT Field Survey Evaluation.....	A.1

## Figures

Figure 2.1. Hanford Site stratigraphy with geologic time scales from Lanigan et al. 2010 (Fig 6.4).	2.1
Figure 2.2. Cold Creek Unit facies and main paleochannels within the Central Pasco Basin (Martin 2010, Figure 3-6).	2.2
Figure 2.3. Multiple buried paleochannels in the Gable Gap area from Bjornstad et al. (2010), Fig 6.3.	2.3
Figure 2.4. Generalized stratigraphic relationship among post-Ringold units for Central Pasco Basin (Figure A.4, DOE 2002).	2.4
Figure 3.1. A typical electrical resistivity tomography (ERT) measurement where a current $I$ is injected across current electrodes C+/C- and the resulting potential field $\Delta V$ is measured across two potential electrodes P+/P-. Photo credit: A. Binley, Lancaster Univ., UK.	3.2
Figure 3.2. A) Schematic airborne EM system and induced vs. measured fields; B) frequency-domain EM primary and secondary fields at receiver; C) time-domain EM transmitter and receiver waveforms (Legault 2015, Figure 1).	3.4
Figure 3.3. Principles of seismic methods (from Schuck and Lange 2007, Fig 4.6-1).	3.7
Figure 3.4. Ground penetrating radar ray paths (from Neal 2004, Figure 4).	3.8
Figure 3.5. Schematic diagram showing the declination (D) and inclination (I) of the total field vector F. Declination is the angle between true north and magnetic north (11.5 degrees). F is caused by the superimposed presence of magnetic minerals and rocks at that location (from Figure 6.12, Haldar 2018).	3.9
Figure 4.1. Comparison of 50-m resistivity depth slice of the RESOLVE FEM survey in a) and the HeliGEOTEM in b) (from Figure 10, Fugro Airborne Surveys 2010).	4.3
Figure 4.2. Ground-based EM-34 model (top) and 2D resistivity model (bottom) (Figure 4-1, Ch2MHill 2010b). The dashed yellow-blue line in both images depicts the water table boundary.	4.4
Figure 4.3. Pre-stack depth-migrated seismic results from a landstreamer survey northwest of 200 East Area interpreting the basalt boundary and potential locations of faults (orange) (Figure 8 from Hyde et al. 2011).	4.5
Figure 4.4. Profile Line 2 was collected along a west-to-east profile north of the LERF basins. The interpreted basalt boundary is shows as dashed dark pink (top) and black (middle, bottom) lines. The Hanford formation is separated into two horizons, an upper (dashed green line) and lower (dashed pink line) (Figure 5, Ch2MHill 2012).	4.6
Figure 4.5. a) Hanford formation thickness estimated from waterborne electrical imaging. Low stage temperature measurements collected on b) 3/31/2009 and c) 8/2/2009. Red contours represent uranium concentrations (Slater et al. 2010, Figure 8).	4.8
Figure 4.6. Plan view ERT image of high stage river water intrusion within the saturated zone. The colored isosurfaces contour the negative changes in EC with respect to baseline conditions, indicating the presence of river water. River water intrusion flows preferentially through two features interpreted as high permeability paleochannels (Johnson et al. 2015, Figure 11b).	4.9

Figure 5.1. The geologic framework model between 200 East and West on the Central Plateau. The Hanford formation has been removed to demonstrate the general shape of a paleochannel between 200 East and West as inferred by areas of lower elevation. .... 5.1

Figure 5.2. Geologic framework model at an elevation of 120 m in the saturated zone. The ERT simulations focus on depths at or below this elevation. .... 5.2

Figure 5.3. a) Potential electrode placement and injection well locations; and b) magnified site view with groundwater flow directions with yellow arrows. .... 5.3

Figure 5.4. The relationship between potassium bromide (KBr) concentration and fluid conductivity (from Isono 1984). .... 5.6

Figure 5.5. A comparison of HEIS nitrate concentrations and fluid specific conductance from boreholes within and surrounding the area between 200 East and West Areas between 12/12/1983 and 11/2/2018. .... 5.8

Figure 5.6. Results of flow and transport simulations of a tracer injection into wells 699-49-69 and MW-10A at elevation 120 m. Shown are aqueous concentrations after the tracer injection ceased 2020 a) 2020.25; b) 2020.5; c) 2021; d) 2025; e) 2027; f) 2034. .... 5.9

Figure 5.7. Flow and transport  $\sigma$  in plan view a) and elevation view b). Background ERT  $\sigma$  images are shown in plan view c) and elevation view with a 5:1 vertical exaggeration d). Color scales are one order of magnitude lower for the ERT  $\sigma$  relative to the flow and transport model  $\sigma$  to highlight the variability in conductivity structure of the ERT  $\sigma$ , which would otherwise not be visible. .... 5.10

Figure 5.8. Time-lapse ERT  $\sigma$  results alongside flow and transport  $\sigma$  conceptual site models. Both models are represented as isosurfaces of logarithmic change from background (year 2020) values. Simulations results are shown after the tracer injection has ceased at a) 2020.25; b) 2020.5; c) 2021; d) 2025; e) 2027; and f) 2034. .... 5.11

## Tables

Table 2.1. Stratigraphic studies<sup>(a)</sup> that specifically mention paleochannels on the Hanford Site. .... 2.4

Table 4.1. Previous geophysical methods used to investigate paleochannels at Hanford. .... 4.11

Table 5.1. Input parameters for flow and transport model simulations. .... 5.4

## 1.0 Introduction

Stratigraphy has typically been mapped on the Central Plateau at the Hanford Site using information from borehole data. These data may include driller, geologist, and borehole geophysical logs, grain-size analyses from sediment samples, as-built diagrams, and/or sediment photographs (Bjornstad et al. 2010; DOE 2002). Representations of the available data include maps of the upper surface elevations or “tops” of the major hydrostratigraphic units interpolated between borehole locations. Where boreholes are sparse or subsurface heterogeneity exists at length scales smaller than the distance between the boreholes, the uncertainty in the interpolation of hydrostratigraphic surface elevations is high. Moreover, data at each borehole may not contain all of these data types, which increases the uncertainty in interpreting among boreholes.

Across the Central Plateau, buried ancestral fluvial channels, or paleochannels, have been inferred from numerous borehole datasets. Paleochannels filled with coarse sediments act as preferential groundwater and contaminant pathways, and therefore can shorten travel times to downgradient receptors (e.g., the Columbia River) while also potentially diluting contaminants to below the maximum contaminant levels. Main paleochannels identified are north of the 200 East Area, which is where the ancestral Columbia River was located, and south of the 200 West Area, the remnant location of Cold Creek. Northwest of 200 East Area, within the Gable Gap area, at least six buried paleochannels have been identified from borehole and seismic datasets, with five carved out from Pleistocene Ice Age floods (Bjornstad et al. 2010). Paleochannels play an important role in contaminant transport across the Central Plateau and delineation of these features is critical to effective environmental management and remediation.

Aside from physical characteristics determined from borehole data, monitoring of contaminant concentrations in groundwater provide indirect evidence of the connectivity of subsurface features in the Central Plateau. An extensive groundwater monitoring program exists on the Hanford Site (DOE 2017) that utilizes thousands of wells whose locations are based in part on source locations and contaminant plume concentrations. Based on the available data, paleochannels have been inferred at several other locations, including southeast of the 200 East Area and in between the 200 East and West Areas. The boreholes in these areas are relatively sparse, and therefore, the interpretation of the geo-hydrology and the impact on contaminant transport predictions between the 200 Areas is uncertain. Improved methods are needed to provide information at a scale consistent with supporting operable groundwater units and remedy implementations.

### 1.1 Geophysical Surveys at Hanford

Previous studies at the Hanford Site have identified several geophysical methods that are fast and cost-effective investigative tools (e.g., Gander et al. 2011; Murray and Last 2005; Strickland et al. 2018). Geophysical methods non-invasively collect measurements in airborne and surface surveys. Depending on the spacing of sensors, resolution can be from centimeter to kilometer scale. On the Hanford Site, stratigraphy interpreted from borehole data has been integrated with surface geophysics to create hydrogeologic models (Bjornstad et al. 2010) and used to validate findings from geophysical surveys collected on or above the ground surface (Ch2MHill 2010a). However, many of the waste management areas at the Hanford Site contain a large amount of metallic infrastructure and electromagnetic sources (e.g., power lines), which has limited the effectiveness of electromagnetic geophysical surveys (e.g., Ch2MHill 2010b). Sources of data noise can be accounted for in some cases, as in a recent re-examination of surface electrical resistivity in the B-Complex (Johnson and Wellman 2013). Buried pipes, tanks, and well casing were explicitly accounted for in the electrical resistivity modeling

performed by Johnson and Wellman (2015), to more accurately predict subsurface distributions of electrical conductivity.

While challenges exist in using geophysical methods on the Hanford Site, these methods have the potential to provide relevant characterization information. For example, although geophysical methods do not provide direct information on grain-size distributions or hydraulic conductivity, relative differences in lithologies can be inferred. Although the magnitude of contaminant concentrations cannot be measured by geophysics, the spatial extent of a plume can be delineated. Geophysical methods are sensitive to physical and/or chemical characteristics in the subsurface. Therefore, the effectiveness of a geophysical method may depend on the characteristics of the target and the goals of the survey.

The purpose of this report is to identify and recommend geophysical methods that may be effective at delineating high permeability paleochannels in the subsurface at the Hanford Site. This was achieved by:

1. Reviewing and evaluating historical field investigations on the Hanford Site where geophysical methods were used to identify lithologic contacts and paleochannels. The review encompasses multiple geophysical methods at varying scales of data acquisition to identify successes and lessons learned in the interpretation of data collected in geophysical surveys.
2. Executing hydrogeophysical simulations to assess the feasibility of using an injected ionic tracer with the geophysical method electrical resistivity tomography (ERT). An ionic tracer is used to enhance the contrast in electrical conductivity between the injected tracer solution and ambient groundwater. The area of interest is between 200 East and West, where a scarcity of boreholes creates uncertainty in the paleochannel spatial extent (Ch2MHill 2016).

## **1.2 Report Organization**

Section 2 of this report provides a brief overview of Hanford Site stratigraphy, focusing on identification of high permeability paleochannels. In Section 3, a review of geophysical methods used at the Hanford Site is provided, followed by a review and evaluation of Hanford geophysical field investigations in Section 4. Computer simulations are used to evaluate the use of ERT for paleochannel identification in Section 5. Preliminary conclusions and recommendations for further evaluating ERT for this activity are provided in Section 6. Based on the ERT evaluation presented in Section 5, a phased approach is provided in Appendix A for obtaining site-specific ERT data and aquifer hydraulic properties.

## 2.0 Hanford Site Geologic Description

The generalized stratigraphy at the Hanford Site (Figure 2.1) consists of five lithostratigraphic units listed here in stratigraphic order from upper (shallow) to lower (deep): eolian and alluvial Holocene sediments (< 1 m thickness); glacio-fluvial deposits associated with cataclysmic ice-age flooding in the Hanford formation; alluvial, fluvial, and paleosol deposits in the Cold Creek Unit (CCU); alluvial and lacustrine deposits in the Ringold Formation; and the Columbia River Basalt Group. These units are subdivided into finer-scale features or facies that depend on the proximity to ancient river systems and floodpaths. Refer to Martin (2010) and DOE (2002) for a complete description of lithology and hydrostratigraphic units.

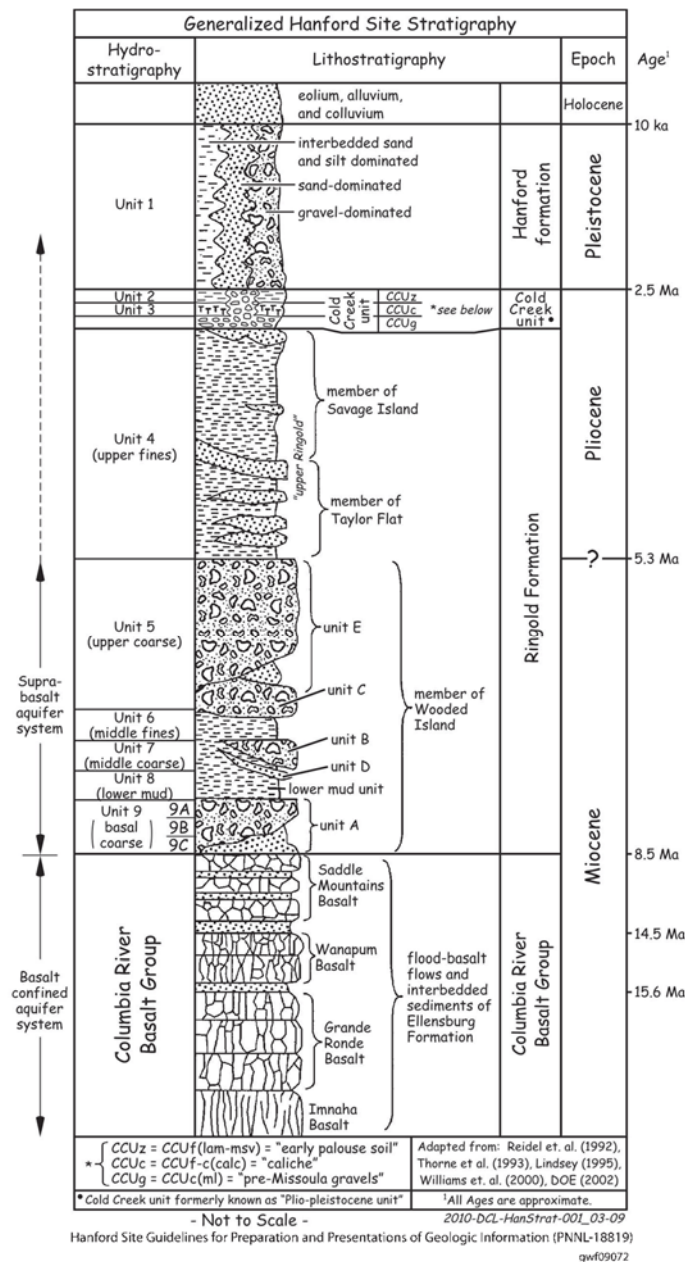


Figure 2.1. Hanford Site stratigraphy with geologic time scales from Lanigan et al. 2010 (Fig 6.4).

Field and laboratory studies have been conducted over a span of decades to characterize the lithology and stratigraphy and hence locate paleochannels at the Hanford Site (Table 2.1). Site-wide paleochannels associated with the ancestral Columbia River and cataclysmic ice-age floods have been identified within the Ringold Formation and the CCU (Figure 2.2). The distribution of CCU units across the Hanford Site and monitored groundwater contaminants can imply where additional paleochannels may be located. For example, a detailed study of the Gable Gap area identified multiple buried paleochannels inferred from dozens of borehole and seismic-reflection data (Bjornstad et al. 2010). Five of the six paleochannels identified (A-E, Figure 2.3) had Ringold sediments removed from extreme erosion that occurred during Ice Age flooding. These paleochannels contain highly permeable Hanford formation deposits.

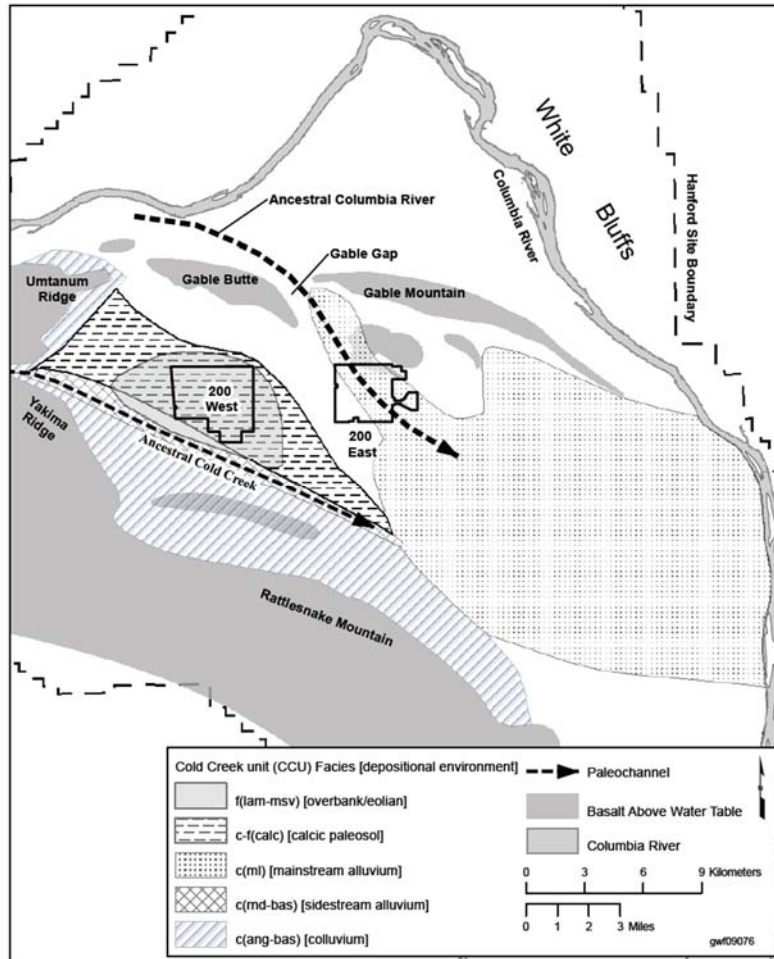


Figure 2.2. Cold Creek Unit facies and main paleochannels within the Central Pasco Basin (Martin 2010, Figure 3-6).

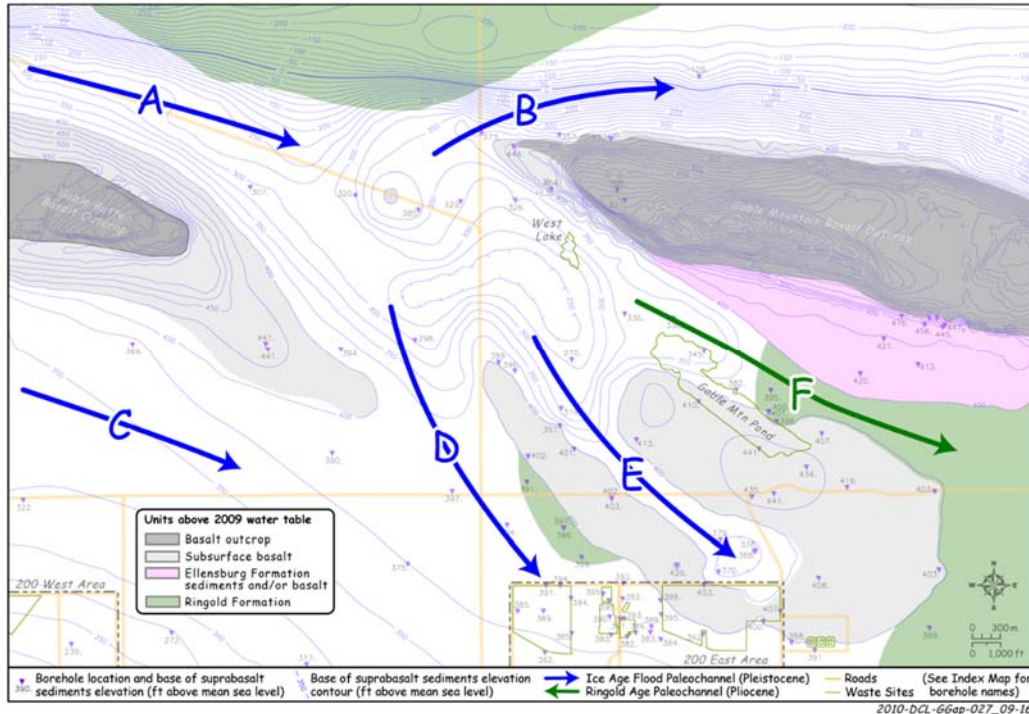


Figure 2.3. Multiple buried paleochannels in the Gable Gap area from Bjornstad et al. (2010), Fig 6.3.

Figure 2.4 shows a conceptual model of a paleochannel in the Central Pasco Basin. This figure includes sediments of the CCU, the Hanford formation, and overlying Holocene deposits. High-energy Hanford formation gravel deposits are shown to have scoured the CCU, and in some places to have direct contact with underlying Ringold Formation or Basalt Group (not shown in diagram). Laterally, a borehole cross section across the 200 West Area showed facies changes within the CCU and Hanford formation (DOE 2002, Figure A-5), suggesting a complex erosional pattern from flow paths of ancestral riverbeds and floods.

The Ringold Formation is divided into six Pliocene- to Miocene-aged facies ranging from coarse to fine-grained sediments. The Ringold lower mud (RLM) unit is a silty layer between coarser facies (refer to Figure 2.1). On the eastern boundary of the 200 West Area, the geologic framework model (Ch2MHill 2016) predicts the RLM is truncated by coarser units, indicating the possibility of transmissive paleochannel within coarser Ringold sediments between 200 East and West Areas.

Table 2.1. Stratigraphic studies<sup>(a)</sup> that specifically mention paleochannels on the Hanford Site.

Report Reference	Year	Title
Fecht et al. 1985	1987	Paleodrainage of the Columbia River System on the Columbia Plateau of Washington State - A Summary
Williams et al. 2000	Apr 2000	Revised Hydrogeology for the Suprabasalt Aquifer System, 200-East Area and Vicinity, Hanford Site, Washington
Williams et al. 2002	May 2002	Revised Hydrogeology for the Suprabasalt Aquifer System, 200-West Area and Vicinity, Hanford Site, Washington
DOE 2002	June 2002	Standardized Stratigraphic Nomenclature for Post-Ringold-Formation Sediments Within the Central Pasco Basin
Bjornstad and Lanigan 2007	Sept 2009	Geologic Descriptions for the Solid-Waste Low Level Burial Grounds
Martin 2010	2010	Chapter 3: Overview of Hanford Hydrogeology
Bjornstad et al. 2010	Sept 2010	Hydrogeologic Model for the Gable Gap Area, Hanford Site
DOE/RL-2011-118, Rev. 0	Aug 2012	Hanford Site Groundwater Monitoring for 2011
Reidel and Tolan 2013	2013	The late Cenozoic evolution of the Columbia River system in the Columbia River flood basalt province

(a) And references therein

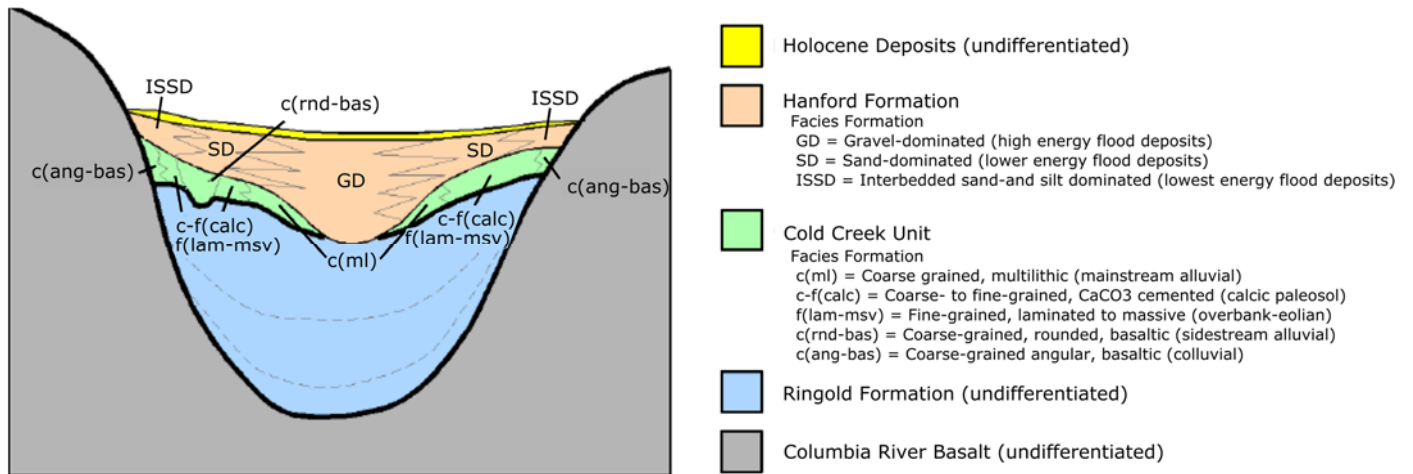


Figure 2.4. Generalized stratigraphic relationship among post-Ringold units for Central Pasco Basin (Figure A.4, DOE 2002).

### 3.0 Geophysical Methods Overview

Geophysical methods measure variations in the electrical conductivity, magnetic susceptibility, seismic velocity, and gravity-induced changes in density using minimally- or non-invasive instrumentation for rapid data acquisition. The relative ease of implementation, low cost, and large interrogation volumes complement and in some cases supplant the labor-intensive, in situ water sampling at monitoring wells. Geophysical methods can provide information at multiple scales (by varying the spacing of sensors), and collect data at field scales needed for characterization and monitoring of groundwater operable units. Additional data (e.g., borehole stratigraphic descriptions, hydraulic properties, aqueous chemical data) can be used in conjunction with geophysical interpretation to better interpret subsurface structure and properties relevant to subsurface flow and transport processes.

To provide context for geophysical surveys performed at Hanford and described in Section 4.0, an overview of relevant geophysical methods is provided here. This review is limited to geophysical technologies that have been used on the Hanford Site and that may be relevant to paleochannel identification. This includes ERT, active source electromagnetics (EM), seismic techniques, ground penetrating radar (GPR), and magnetics. The following methods, however, are not considered in this review because they are not considered relevant to paleochannel characterization:

- **Single borehole methods (e.g., geophysical borehole logging).** Borehole geophysical data has the same limitation as more traditional borehole datasets: The spatial information is limited to the region surrounding the borehole and identification of a paleochannel is through interpolation of these datasets. While borehole datasets can be used to ground-truth other datasets, the objective here is to identify geophysical methods that can be used for paleochannel identification at a regional scale.
- **Magnetotellurics (passive source electromagnetics).** This is typically used for deep investigation (>100 m) and is not applicable to paleochannel identification on the Hanford Site, where the relevant depth is within the top 100 m.
- **Surface nuclear magnetic resonance (NMR).** This method, while excellent at detecting subsurface fluid and saturation variations, is extremely sensitive to ambient electromagnetic noise. The magnitude of the noise can often exceed the magnitude of the NMR signal (Behroozmand et al. 2014). Until there are improvements in hardware and software-based signal processing to remove this unwanted signal, the ambient noise (e.g., power lines) on the Hanford Site makes this method impracticable.
- **Gravity / Microgravity.** Gravity as a geophysical method is sensitive to density contrasts in the surface. ASTM Standard D 6429-99, *Selection of Geophysical Methods for Common Applications* (ASTM International 1999), defines voids and sinkholes, fractures and fault zones, and bedrock depths as good targets for gravity surveys. At the Hanford Site, gravity was used to identify buried bedrock features to understand the geology of the Pasco Basin (Richard et al. 1977). More recently, density within three boreholes was measured with a gravity survey at the Hanford Waste Treatment and Immobilization Plant for seismic modeling (MacQueen and Mann 2007). However, beyond borehole investigations, gravity as a geophysical technology at the Hanford Site deemed site noise a limiting factor (Murray and Last 2005). There are no recent uses of gravity that capture information at the spatial extent needed for paleochannel identification and this is presumably due to site noise and/or lack of sensitivity to the density contrasts of paleochannels.

This method overview section is not intended to be comprehensive, but references are provided for readers interested in obtaining more detailed information on the geophysical methods.

### 3.1 Electrical Resistivity Tomography

ERT is sensitive to bulk electrical conductivity (the inverse of electrical resistivity) in the subsurface. Electrical conductivity is affected by physical properties including lithology, pore water fluid conductivity, porosity, moisture content, and temperature. ERT is an active source geophysical method where an electric potential field is generated in response to a current injection  $I$  across two transmitting electrodes (Figure 3.1). The resulting change in potential  $\Delta V$  is recorded across two receiving electrodes (Ward 1988). Assuming low surface conduction, electrolytic current pathways closely mimic hydraulic pathways and distributions of electrical conductivity can be used to infer subsurface structure or migration of an ionic fluid (Falzone et al. 2018). Electrical measurements are correlated to pore fluid properties (i.e., salinity, saturation) and lithology (i.e., porosity).

The spacing between the transmitting and receiving electrodes determines the spatial resolution and volume of interrogation over which each measurement is collected. The spacing between electrodes can range from a few centimeters up to hundreds of meters. Electrodes with spacings that are farther apart sample a larger volume with lower spatial resolution. In comparison, closer spaced electrodes sample a smaller volume with higher spatial resolution. The interrogation volume is highly scalable depending on the spacing of electrodes.

ERT measurements can be collected on the surface or in boreholes. Surface electrodes are typically metal rods that penetrate the ground surface several centimeters or as shallow as necessary to have electrical contact with the subsurface. Borehole electrodes can be installed along the outer diameter of non-metallic well casing as low-profile metal clamps or within an open well using metallic electrodes along an electrical cable (Robinson et al. 2015). If the installation is below the water table, contact with the formation is maintained through the groundwater fluid. In vadose zone studies using well casing, electrical contact with the formation is maintained via the backfill or grout in the borehole annulus.

Once electrodes are installed, they can be left in place to monitor changes from an initial state (Singha et al. 2014). Time-lapse ERT methods offer an advantage over other geophysical methods because the competing effects of lithology, porosity, etc. can be eliminated by focusing on changes in electrical conductivity rather than on absolute conductivity.

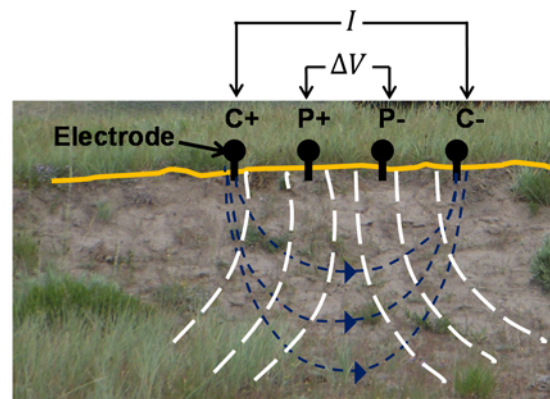


Figure 3.1. A typical electrical resistivity tomography (ERT) measurement where a current  $I$  is injected across current electrodes C+/C- and the resulting potential field  $\Delta V$  is measured across two potential electrodes P+/P-. Photo credit: A. Binley, Lancaster Univ., UK.

#### 3.1.1 Induced Polarization

An induced polarization (IP) survey measures the stored charge or polarization response of an injected current in the subsurface and is highly dependent on mineral surface area. Given the high sensitivity to mineral surface area, field IP surveys have the potential to more clearly identify lithological variations inferred from ERT results, which provides a more robust interpretation. In all cases, IP data are collected at the same time as an ERT survey: An ERT survey measures  $\Delta V$  after shutoff of an injected current and

an IP survey measures the voltage-decay (time-domain) or phase-lag (frequency-domain). For some systems, the additional data collected from an IP survey results in additional data collection time, which can be prohibitive factor in some cases. When IP measurements are collected at multiple frequencies, it is referred to as spectral IP, or SIP.

Electromagnetic coupling can be a major obstacle in the interpretation of IP data (Routh and Oldenburg 2001). These effects can be observed at frequencies as low as 1 Hz but typically occur at higher frequencies ( $> 10$  Hz). Capacitive coupling, which can arise from a leakage of displacement currents between transmitter and receiver wires or transmitter wires and the ground (Wynn 1974), can be minimized by separating the current and potential cables (Dahlin and Leroux 2012). Inductive coupling can manifest between wires or through induction within the earth and is more pronounced in conductive environments or where dipole lengths are large. While quasi-filtering (Binley 2015) and numerical solutions (Routh and Oldenburg 2001; Zhao et al. 2015; Kemna et al. 2014) have been proposed, more research needs to be done to characterize these effects if they are observed in a dataset.

## 3.2 Active Source Electromagnetics

Like ERT, EM is sensitive to bulk electrical conductivity in the subsurface. EM surveys are performed on or above the surface by passing a current through a transmitting wire coil, which then propagates a primary electromagnetic field above and below the ground. The magnetic component of the EM wave induces eddy currents in subsurface conductive material, producing a secondary EM field. Secondary EM field(s) are detected by a wire coil receiver and can be distinguished from the primary field (Figure 3.2). Secondary EM fields provide information about the geometry, size, and electrical properties of subsurface conductors.

EM systems are typically categorized by the positioning and/or layout of the transmitter and receiver. Small-loop EM systems are composed of a multiple or multiples of two small coplanar coils (i.e., a transmitter and receiver) separated by a fixed distance. These systems are moved along acquisition lines at a known position. The lengths of these systems can vary from 1 to 10 m, and can be held by an operator, mounted on a motorized vehicle, or deployed by airborne systems (e.g., mounted on a helicopter). Large-loop EM systems contain a polygon-shaped (e.g., square or hexagon) transmitter loop (5 to 200 m side length) consisting of a single conductor wire and a receiver antenna centered within the transmitter loop. These systems can be laid out on the ground or suspended from a helicopter (Figure 3.2) or small plane for an airborne survey.

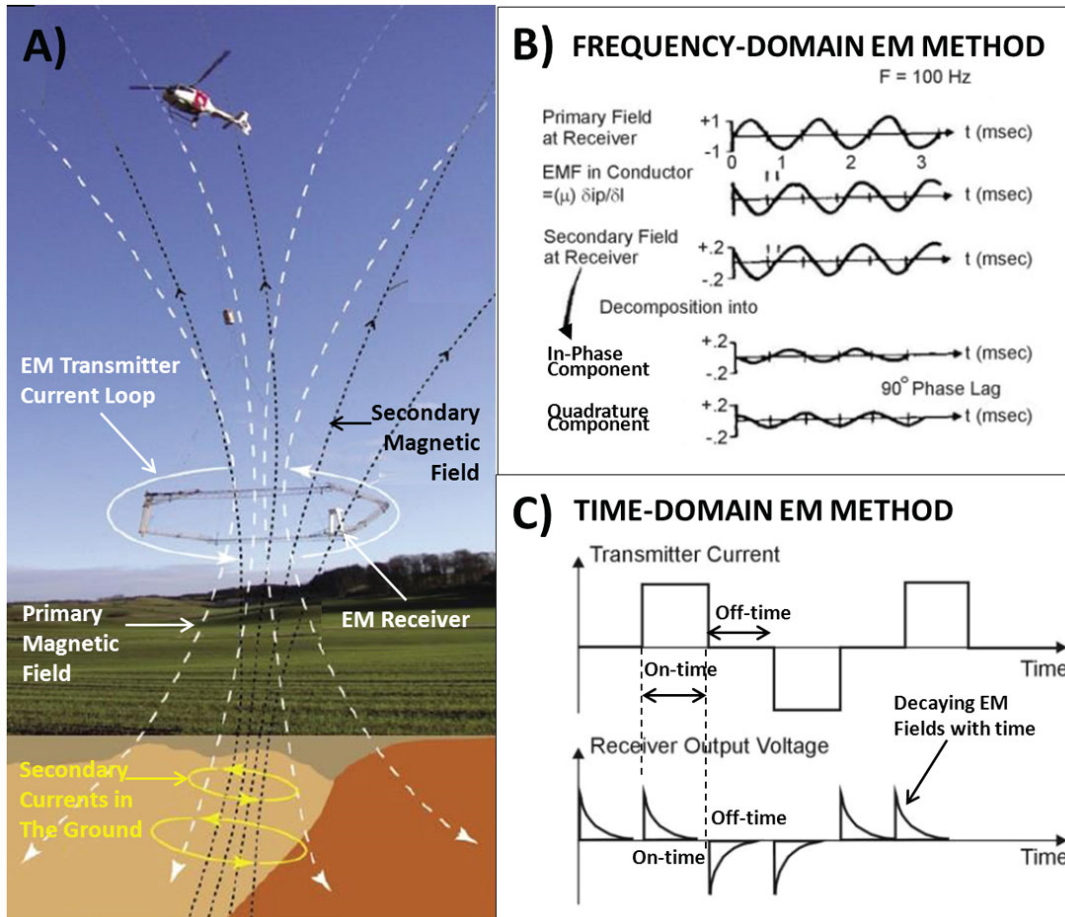


Figure 3.2. A) Schematic airborne EM system and induced vs. measured fields; B) frequency-domain EM primary and secondary fields at receiver; C) time-domain EM transmitter and receiver waveforms (Legault 2015, Figure 1)

Measurements can be collected as a function of time, for time-domain EM (TEM or TDEM), or at one or more frequencies, for frequency-domain EM (FEM or FDEM). In TEM, the transmitter emits a short duration symmetrical square wave voltage pulse and the secondary field is measured as the amplitude of the decay over time. Measurements at successively later times provide information at greater depths. The same coil can be used as the transmitter and receiver, but more often a separate receiver coil centered within the transmitter loop is used.

In FEM, the secondary field is commonly reported as the real or in-phase component and the quadrature or out-of-phase component. The in-phase component is responsive to discrete, highly-conductive objects such as metal. In the absence of highly conductive objects, the magnitude of the in-phase component depends on the magnetic susceptibility. Using simplifying assumptions, the quadrature component is linearly proportional to the apparent conductivity of the subsurface.

The depth of exploration is a function of the time or frequency of the EM field and the electrical conductivity of the medium. The skin depth  $\delta$ , defined herein as the depth at which the amplitude of a plane-wave electromagnetic field reduces to  $1/e$  (0.378), is a common measure used to determine attenuation from the Earth's surface (Spies 1989):

$$\delta = \sqrt{\frac{2}{\sigma\mu\omega}} \quad (3.1)$$

where  $\sigma$  is the electrical conductivity,  $\mu$  is the magnetic permeability, and  $\omega$  is the angular frequency (where  $\omega = 2\pi f = 1/t$ ). Eq. (3.1) assumes  $\sigma$  and  $\mu$  are frequency independent and that displacement currents can be ignored. Skin depth can be used as a first-order estimate of penetration depth. As shown in Eq. (3.1), as frequency and electrical conductivity increase, skin depth decreases. For airborne surveys, geometrical attenuation must also be considered in addition to frequency dependence. To this end, Beamish (2004) defined a vertical decay scale length, called a dipolar skin depth and compared these results with plane-wave [Eq. (3.1)] skin depths. It was found that dipolar skin depths were much smaller than plane-wave skin depth except at frequencies  $> 50$  kHz. Therefore, airborne EM survey skin depth estimates using Eq. (3.1) could potentially overestimate depth.

EM has several notable advantages over ERT, including faster data acquisition over larger areas and in land, air, and sea environments. Since EM is based on induction, the method does not require electrode contact with the ground. Disadvantages include a fixed depth of investigation based on the instrumentation frequency(ies), the transmitter and receiver coil separation, and noise from non-geologic objects such as power lines and buried metallic objects.

### 3.3 Seismic

Seismic techniques exploit the propagation of elastic energy in the subsurface and generally involve measuring the travel time of low-frequency acoustic energy from a source location, called a shot point, to motion sensors, called geophones, which transform seismic energy into an electrical voltage (Pelton 2012). From the surface, a seismic wave spreads out hemi-spherically into the subsurface, causing different particle motion orientations, which are used in the naming convention. Particle motions that are parallel and perpendicular to the direction of seismic wave propagation are compressional or ‘P’ waves and shear or ‘S’ waves, respectively. S-waves travel slightly slower than P-waves in solids and can only propagate in material that have shear strength. P- and S- waves are also referred to as body waves since they penetrate the interior of the Earth. Surface waves travel primarily along the ground surface or at shallow depths and are characterized by elliptical motion perpendicular to the surface (Rayleigh waves) or perpendicular to the propagation direction (Love wave).

Acoustic energy sources are typically explosives, a weight drop, vibrators, or gas/air guns and shot locations depend on survey objectives. On the surface, seismic surveys can be performed with stationary source and receiver locations or with towed arrays using gimbaled geophones. Within a borehole, seismic data can be obtained within a single borehole using a surface source location to a known depth (check-shots) or along an entire vertical profile. These data are often used with borehole geologic information and correlated to surface seismic data. Additionally, cross-well seismic tomography can be performed where a source is lowered in one borehole and stationary receivers in another borehole record the arrival of the seismic wave (Figure 3.3).

P- and S-body waves are refracted or reflected at interfaces with different velocities and/or densities (Figure 3.3). This signal is recorded in conventional reflection (Steeple 2005) or refraction surveys where the offset of sensors controls the investigation depth. In near-surface investigation, reflection survey depths can range from ten to hundreds of meters. For refraction surveys, the near-surface investigation depth can be less than 30 m, due in part to the length requirement of the array must be at least 5 times the desired depth of interest. While refraction surveys are generally less expensive, reflection

surveys have better vertical resolution and are better to identify deep, small targets (Rabbel 2010). The wave velocities of P-waves and S-waves can be readily obtained to solve for engineering properties such as Young's modulus (E), shear modulus (G), and either density or Poisson's ratio ( $\nu$ ).

Measurements of Rayleigh surface waves, also known as ground roll, can provide dispersion properties of the seismic wave as profiles of shear wave velocity. Spectral or multichannel analysis of surface wave surveys (SASW or MASW, respectively) can be used to determine 1D or 2D vertical profiles of shear wave velocity (Lin et al. 2017; Park et al. 2007) for soil profiling or depth to a basement basalt layer (Yaede et al. 2015). Typically, SASW and MASW surveys have a shallower depth of exploration than conventional reflection and refraction surveys.

Regardless of the type of seismic wave surveyed, the same methodology is used for each survey with different geometries and data processing procedures. The data are typically stacked (i.e., multiple traces are acquired and added together) to boost the signal to noise ratio. Raw seismic data collected from the surface cannot account for dipping reflectors or complex geology. Therefore, data migration is often performed, a process in which seismic data are geometrically re-located in either space (depth) or time. Depth migration is better at resolving lateral velocity variations; however, a velocity model is required to convert travel time to depth coordinates. Both pre- and post-stack migration can be performed. Seismic inversion is used to transform seismic data into a quantitative rock property, impedance, which is equal to the multiplication of sonic velocity and bulk density.

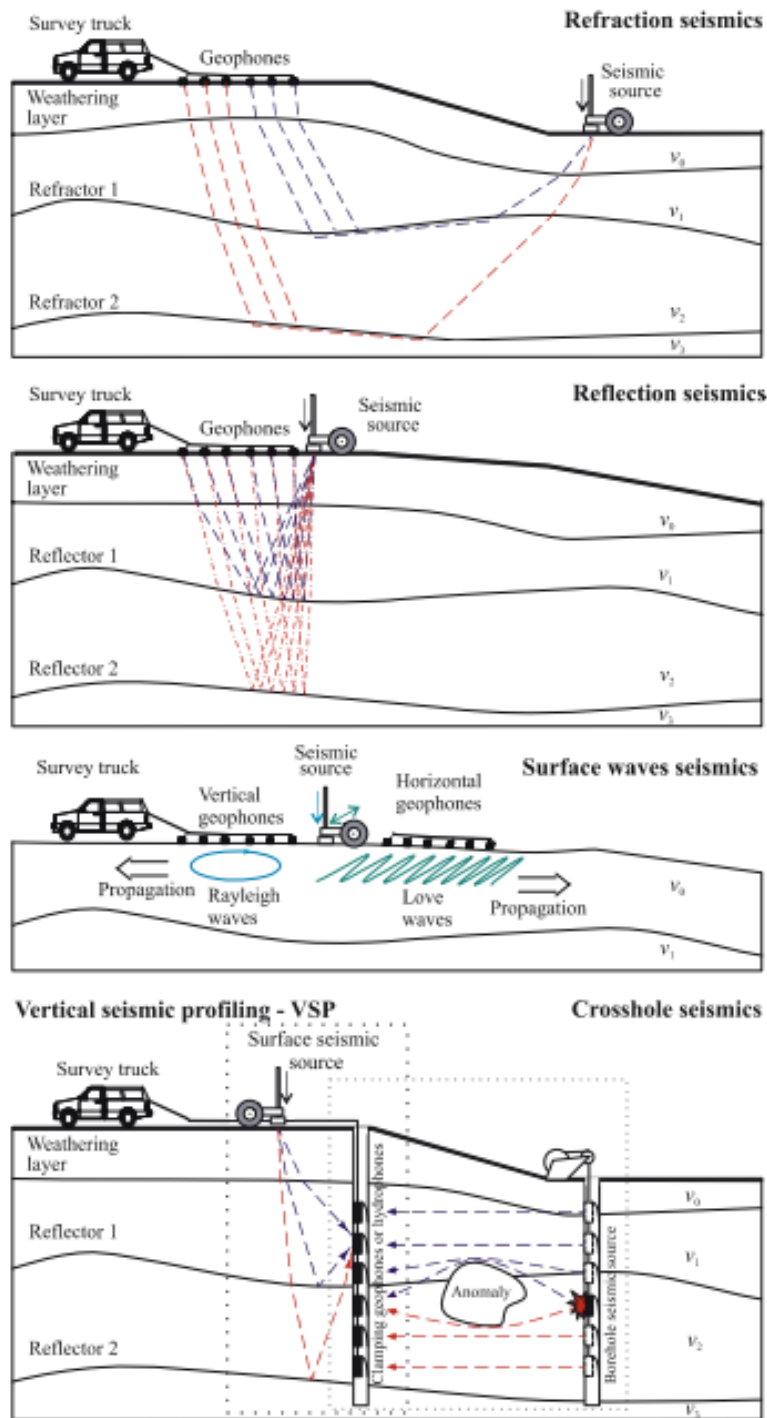


Figure 3.3. Principles of seismic methods (from Schuck and Lange 2007, Fig 4.6-1).

### 3.4 Ground Penetrating Radar

GPR is a shallow geophysical technique that uses the transmission and reflection of high frequency (10 MHz to 1 GHz) EM energy (Annan 2009). Surface-based GPR data are acquired by sending an alternating pulse of EM energy into the earth from a transmitter antenna located at the earth's surface and recording energy that is reflected back to a receiver antenna also located at the surface (Figure 3.4). The most common survey technique is called the common offset, where the transmitter and receiver antennae have a fixed spacing. A radar image is a display of the arrival time and amplitude of the air wave, ground wave, and refracted and reflected energies. Reflected energy is from interfaces in the subsurface across which there are changes in dielectric properties, so the radar image is, in part, a representation of the variation in the dielectric properties of the subsurface. Radar images capture information about the large-scale architecture of the subsurface, and also smaller-scale spatial variation.

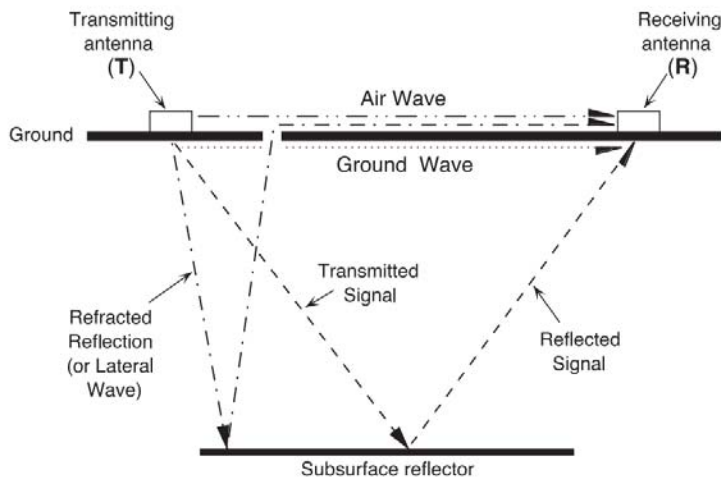


Figure 3.4. Ground penetrating radar ray paths (from Neal 2004, Figure 4).

Dielectric permittivity is measured in units of electrical capacitance (farads) per meter and represents the ability of a material to store electrical charge (Neal 2004). Lateral resolution and penetration depth are inversely related: The higher the frequency, the better the lateral resolution and the lower the depth of penetration. At lower frequencies, the lateral resolution is less resolved but with better depth of penetration (e.g., Smith and Jol 1995). Propagation of an EM wave in the subsurface depends not only on the dielectric properties (which are to some extent frequency dependent) but also the electrical conductivity

and magnetic permeability. In highly conductive environments (e.g., high clay content), energy losses can significantly reduce the penetration depth. Electrical conductivity has the greatest influence over signal attenuation.

Within the megahertz to gigahertz bandwidth, the permittivity of water is approximately 80, air is equal to 1, while most other subsurface constituents are between 3 and 10. This large contrast makes GPR especially well-suited for estimating water content (Vereecken et al. 2008). Two commonly used relationships to estimate soil water content are a model proposed by Topp (1980) and the Complex Refractive Index Model (CRIM) (refer to Huisman and Hubbard 2003). Topp (1980) established an empirical relationship between measured permittivity and volumetric water content for a variety of mineral soils. CRIM is a mixing model that uses the volumetric fractions and dielectric permittivity of each soil constituent.

### 3.5 Magnetics

The magnetic geophysical method measures magnetic variations in the subsurface, which are primarily due to the presence of the Earth's magnetic field. The Earth's magnetic field is a dipole where magnetic field lines run from the South Pole (positive) to the North Pole (negative), inducing magnetism within

rocks. Ferromagnetic minerals also create a magnetic field that may not be in alignment with the Earth's magnetic field. Known ferromagnetic materials are iron, nickel, cobalt, and alloys with titanium and aluminum (Spain and Venkatanarayanan 2014). Magnetism is measured as the sum of all magnetic fields measured in tesla (T) (Figure 3.5). Magnetic susceptibility ( $k$ ) describes the ability of a rock to be magnetized and is the parameter of interest from magnetic data. The dimension of  $k$  is unitless and is the ratio of magnetization (the magnetic moment per unit volume) to the applied magnetizing field intensity.

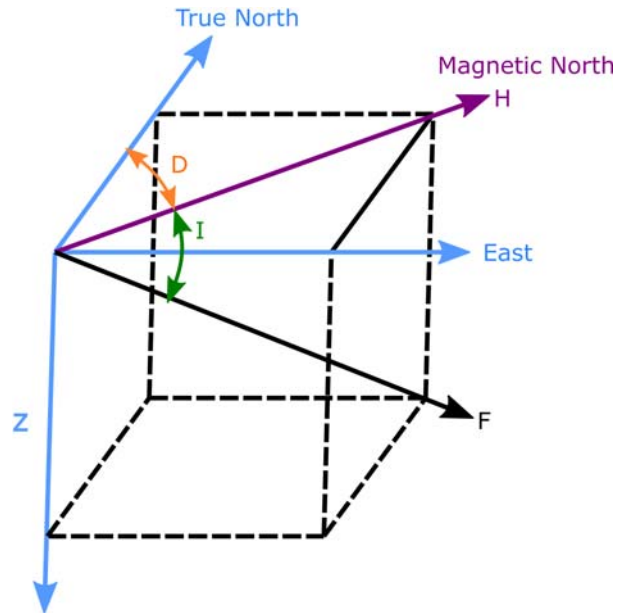


Figure 3.5. Schematic diagram showing the declination ( $D$ ) and inclination ( $I$ ) of the total field vector  $F$ . Declination is the angle between true north and magnetic north (11.5 degrees).  $F$  is caused by the superimposed presence of magnetic minerals and rocks at that location (from Figure 6.12, Haldar 2018).

Measurements can be acquired from hand-held instruments in a laboratory, the ground surface, in boreholes, in airborne and ocean surveys, and in space. Magnetic fields external to the Earth have a large effect on magnetic measurements and these must be removed during post processing (Nabighian et al. 2005). These include solar winds and diurnal fluctuations from the sun. Latitude corrections are also necessary to account for the different inclinations of the magnetic field lines (Blakely 1996).

Magnetics has been extensively used for oil and gas exploration to detect faults and igneous intrusions, metallic mineral exploration (Haldar 2018), and archeological explorations to detect buried structures (Bevan and Smekalova 2013). Magnetostratigraphy is a term used to describe how magnetic data provide chronology in strata independent of fossil content by correlating magnetic reversals of sediments with known temporal pole orientations (Reynolds 2002). Magnetostratigraphy has been used to record a complete reversal in the magnetic field of Miocene lava flows at Steens Mountain in southeastern Oregon (Mankinen et al. 1987). Pluhar et al. (2006) used Cold Creek bar sediments in the Pasco Basin (Washington State, USA) to determine three glacial maxima during the early Pleistocene, providing a more complete record on this time period.

Most sedimentary rocks contain negligible amounts of magnetic material, while igneous and metamorphic rocks can contain appreciable amounts. At the Hanford Site, basalt has a large magnetic signature and can be used to distinguish the EM response as originating from basalt or sediments and overburden. In addition, man-made iron and steel drums have a high magnetic susceptibility and represent strong targets for this method.

## 4.0 Previous Geophysical Work Done to Identify Preferential Flow Pathways at Hanford

A number of geophysical surveys have been executed in both the unsaturated and saturated zones at Hanford with the goals of characterizing subsurface properties or locating contaminants (e.g., Geomatrix Consultants Inc 2005; Last and Horton 2000; Murray and Last 2005; Strickland et al. 2018). Since this report is focused on identification of stratigraphic features, and in particular paleochannels, this report is limited to geophysical investigations performed for this purpose. Large-scale field campaigns (on the order of kilometers) have used EM and seismic methods, and ERT has been used to corroborate the findings from these campaigns. Therefore, the sections below focus on these large-scale applications using EM, seismic methods, and ERT both independently and in conjunction with other methods. Table 4.1 summarizes the studies performed to investigate paleochannels within the stratigraphy.

### 4.1 Electromagnetics and Integration Investigations

Most of the land-based field work using EM methods at Hanford has been for detection and mapping of underground pipelines, utilities, buried debris, and other structures that are primarily metallic or conductive materials (Last and Horton 2000). EM measurements have also supplemented magnetic gradiometer data to better locate shallow underground metallic objects (Rucker et al. 2007; Myers et al. 2009). Land-based TEM has also been used more recently to detect pipeline leakages. For example, Fink et al. (2010) found that high conductivity zones from ERT were coincident with those detected from ground-based TEM to locate leakages. These investigations, while promising, were shallow in scope, imaging in the top 20 m.

In 2008 within the 200-PO-1 groundwater operable unit (OU) of the 600 Area, two airborne EM (TEM and FEM) datasets and magnetic surveys were collected to map lithological changes in the upper layers (top 50 to 150 m), detect possible paleochannels, and locate structural breaks. Magnetic surveys were conducted in parallel and were used to decipher signatures from the basement basalt bedrock and features within sediments and overburden. Power lines and cultural interference were a major concern in these datasets. Paleochannels were assumed to be more resistive, channel-like features infilled with coarser-grained deposits (Ch2MHill 2010b); however, EM is most sensitive to high conductivity zones. This made identifying laterally continuous resistive zones challenging.

Apparent resistivity models were calculated for both surveys, although it is unclear if the same method was used to produce these models. The TEM reports using a simple plate in free space model (Dyck and West 1984), while the FEM survey reports using a pseudo-layer half-space model (Fraser 1978), which consists of a resistive layer overlying a conductive half-space. The apparent resistivity models output an apparent depth, which was corrected for each section to the true topographic surface elevation. For these topographically corrected models, apparent resistivity-depth (or the so-called differential resistivity-depth as described by Huang and Fraser 1996) slices were generated at 10-m intervals. Further details of the surveys performed are as follows:

1. HeliGEMTEM survey (Fluor Hanford Inc. 2008a): A total of 55 north-south lines were collected with a nominal spacing of 400 m. Line lengths varied from 7 to 21 km and the receiver was flown at 47 m above the ground at survey speed. Using a multi-coil system (x, y, and z), 20 data-time windows were collected starting at 0.067 ms and ending at 16.667 ms.

A database of 60 levels of apparent resistivities were prepared ranging from 0 to 590 m below the

surface at 10-m intervals. The effective depth of penetration is reported as 250 m. Due to the broad footprint of the HeliGEOTEM, changes in resistivity every 10 m were gradual; therefore, three averaged resistivity depth slices were prepared to present shallow (40 m: averaged from 20, 40, and 60 m), middle (100 m: averaged from 80, 100, and 120 m), and deep (160 m: averaged from 140, 160, and 180 m) layers.

Generally, the lower resistivity in these profiles was correlated with the Ringold and Ringold Lower Mud units. Zones of lower resistivity are not continuous and this was interpreted as a geologic control, either the location of a fault or a paleochannel.

2. RESOLVE FEM survey (Fluor Hanford Inc. 2008b): This survey had a smaller aerial footprint, and imaged shallower than the HeliGEOTEM survey, resulting in higher resolution output. Flight lines were flown suspending the instrument at 30 m above land surface in an azimuthal direction of 2 degrees with line separations of 100 m and 200 m. A multi-coil coaxial/coplanar source energizes conductors in x, y, and z directions. The RESOLVE system contains five coplanar (horizontal) oriented coils with frequencies of 400, 1800, 3300, 8200, 40,000, and 140,000 Hz. There was also one coaxial (vertical) coil with a frequency of 3300 Hz. The system produces an in-phase and quadrature measurement from each transmitter-receiver coil pair. The effective depth of penetration is reported as 60 m.

To interpret the recorded FEM data, differential resistivity-depth slices were produced from 2 to 52 m at 10-m intervals using a pseudo-layer half-space approximation of the subsurface (Fraser 1978). However, this approximation to a 3D earth has limitations and might not produce the true resistivity distribution. Therefore, to accurately interpret the recorded EM data, a full 3D inversion of the recorded EM data is required.

A comparison of the results is shown in Figure 4.1, as resistivity depth slices at 50 m, representing a shallow image from the HeliGEOTEM and a deep image from the RESOLVE survey. The color scale is shown for comparative purposes only (Figure 10, Fugro Airborne Surveys 2010). Although the RESOLVE survey is more detailed, the images generally show agreement in the location of resistive features interpreted as paleochannels or preferential flow pathways. However, the depths reported for the slices are not true depths; rather, they represent the location where the strongest EM signal is being generated as the signal decays within the subsurface (Ch2MHill 2010b). This generalizes the comparison shown in Figure 4.1 and introduces ambiguity in interpreting these (depth-located) results.

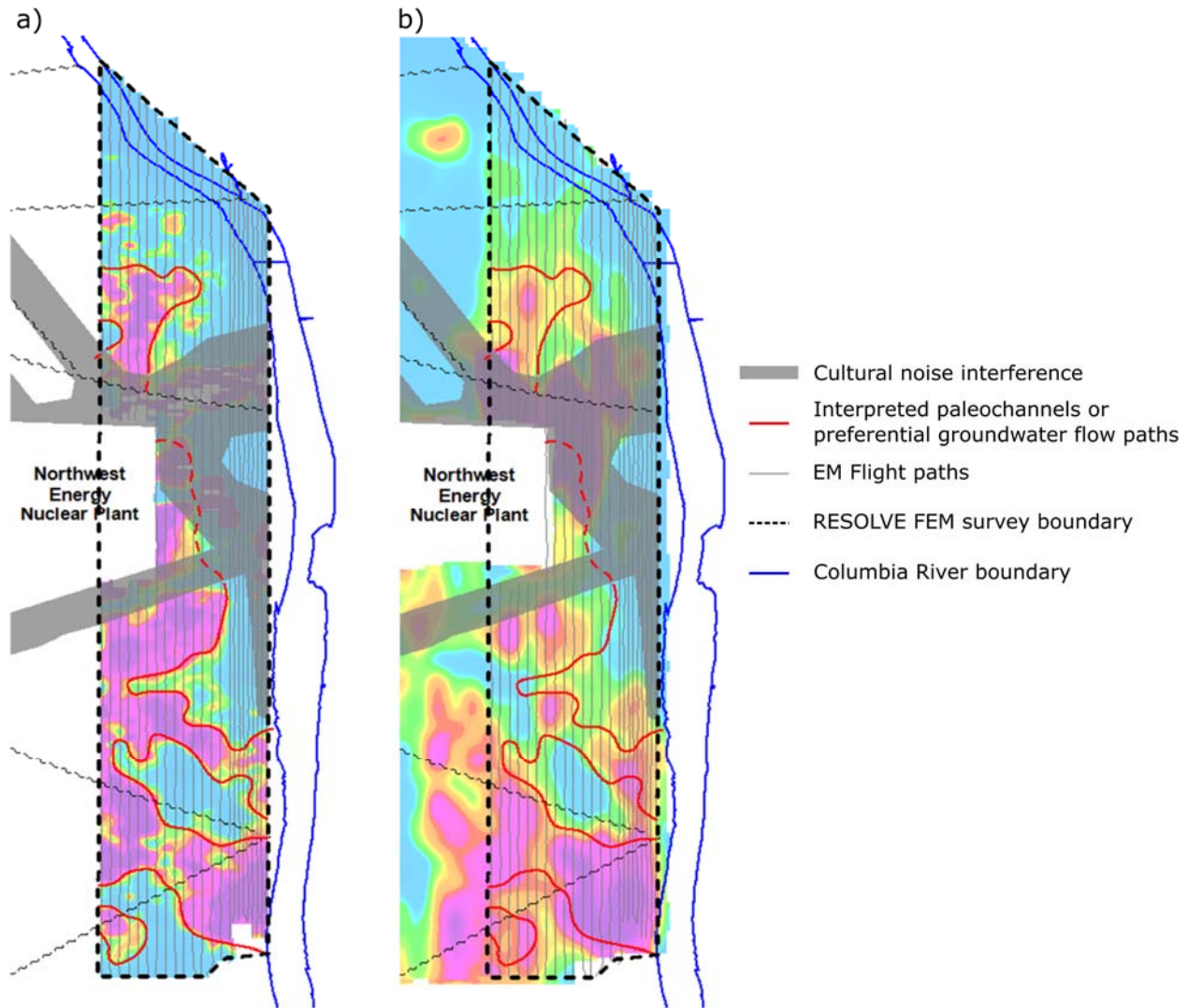


Figure 4.1. Comparison of 50-m resistivity depth slice of the RESOLVE FEM survey in a) and the HeliGEOTEM in b) (from Figure 10, Fugro Airborne Surveys 2010).

Ground-based FEM and 2D ERT techniques were used to compare and contrast to the Ch2MHill (2010a) analyses. An EM survey was performed using a Geonics EM-34 with three frequencies (400, 1600, and 6400 Hz) to compare with airborne EM data. The manufacturer reports horizontal dipoles have an effective depth ranging from 6.5 to 26 m; the effective depth of vertical dipoles ranges from 1.5 to 32 m. One-dimensional layered earth models using three layers were used to construct a 2D cross-section.

A roll-along 2D ERT survey was used by overlapping 84 electrodes spaced at 6 m for a total profile length of 5538 m. A 2D constrained inversion using the commercially available software RES2DInv accounted for the water table, providing a sharp contrast at this depth within the modeling. An investigation depth of 80 to 120 m was reported for the survey type used and electrode spacing.

The ground-based FEM and 2D ERT (Figure 4.2) identified changes in resistivity and likely geologic contacts (Hanford-Ringold, intra-Ringold). The Hanford-Ringold contact was found as a high-to-low change in resistivity magnitude. Both methods imaged the transition from unsaturated to saturated conditions.

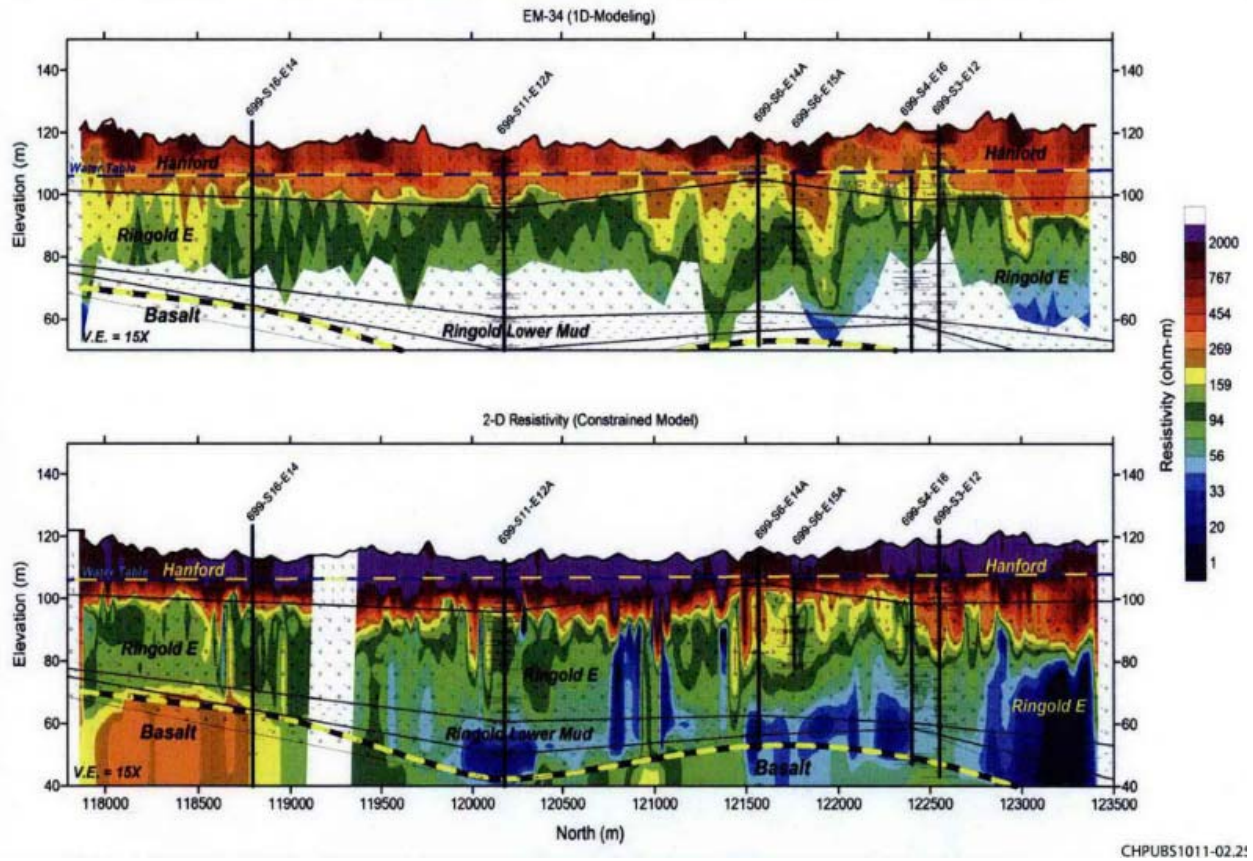


Figure 4.2. Ground-based EM-34 model (top) and 2D resistivity model (bottom) (Figure 4-1, Ch2MHill 2010b). The dashed yellow-blue line in both images depicts the water table boundary.

Comparing ground-based methods with the HeliGEO TEM and RESOLVE airborne surveys, the following was found (Ch2MHill 2010a):

- The depth of the Hanford-Ringold contact was identified as shallower for the ground-based FEM system. The 2D ERT identified the Hanford-Ringold contact as a change from higher resistivity (250 ohm-m) to lower resistivity (< 150 ohm-m).
- The ground-based FEM system mapped the near surface, highly resistive vadose-zone sediments better. The authors concluded that the near-surface vadose zone sediments were not correctly imaged in the RESOLVE FEM survey, due to the very high resistivities (>1500 ohm-m), which was below the sensitivity range of the RESOLVE instrument.
- The HeliGEO TEM has the lowest resolution and inverse modeling was recommended to compare with the underlying geology.

## 4.2 Seismic and Integration Investigations

Seismic methods were employed north of the 200 East Area within Gable Gap to refine the groundwater flow model and identify when northerly flow conditions through the gap and easterly flow conditions south of the gap occurred. The objective of these surveys was to map the top of basalt layer and possible erosional channels within the suprabasalt sediments that dictate groundwater flow direction.

In 2009, a high-resolution seismic landstreamer / gimbaled survey (Ch2MHill 2009) was deployed, consisting of eight profiles with total length of 11 km. The data was evaluated for the depth and geometry of reflectors. Processing included pre- and post-stack time migrations, and pre-stack depth migration, constrained by borehole check-shot surveys to known geologic units. Geologic velocity functions were used to convert travel time to elevation for depth migration. The top of basalt was a recognizable seismic reflection on the raw data. Profiles revealed a highly variable depth profile of the top of the basalt. Erosional channels were inferred as depressions in 3D views (Figure 4.3). The smallest channel this survey is capable of detecting reliably is reported as 10 m thick and 20 m in width.

In 2011, a re-evaluation of previously collected high-resolution seismic datasets was performed (Ch2MHill 2011) to map the top of basalt and suprabasalt contacts. The datasets included the 2009 landstreamer data, data collected in FY 2008 within the 200 East Area, and during FY 1979 and FY 1980 as part of the Basalt Waste Isolation Project. Check shots (i.e., seismic data obtained within a single borehole using a surface source location to a known depth) were the primary method used to correlate seismic data with the geology. These surveys demonstrated seismic was capable of resolving interfaces within the vadose zone sediments of supra-basalt sediments, including Hanford subunits and the Cold Creek and Ringold units.

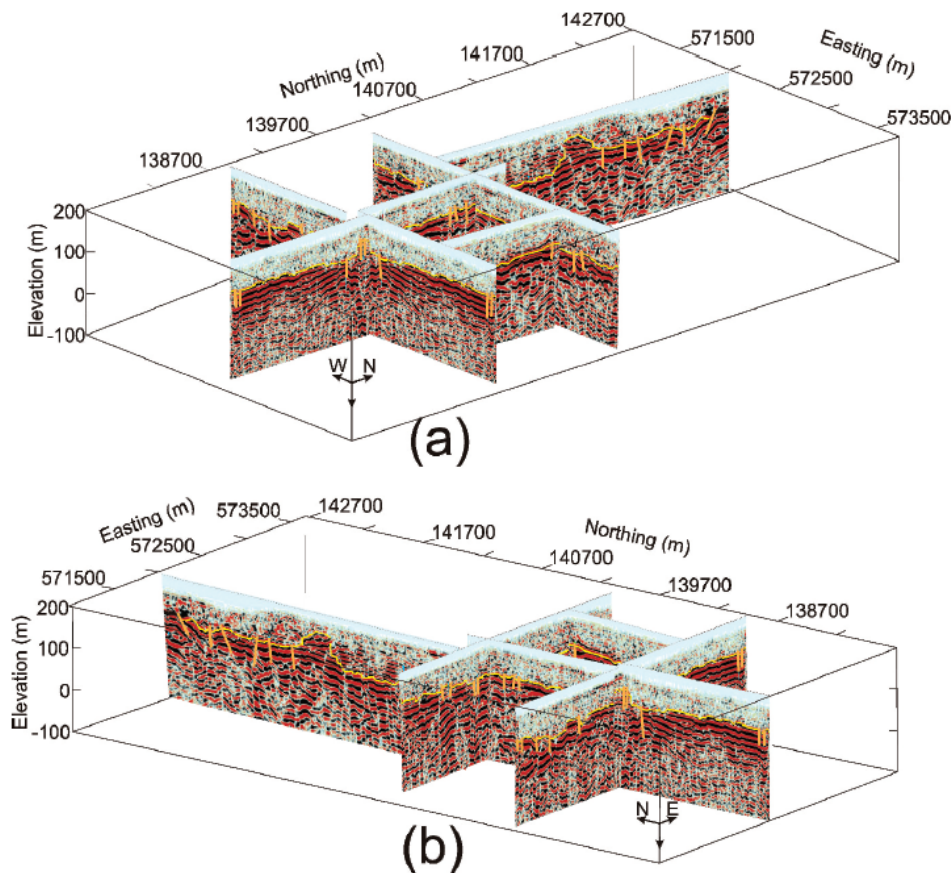


Figure 4.3. Pre-stack depth-migrated seismic results from a landstreamer survey northwest of 200 East Area interpreting the basalt boundary and potential locations of faults (orange) (Figure 8 from Hyde et al. 2011).

Another integrated approach at the Liquid Effluent Retention Facility (LERF) used seismic refraction, vertical seismic check shots, 2D ERT, and TEM 1D soundings to provide supporting information for

locating a future groundwater monitoring well (Ch2MHill 2012). The surveys were focused on imaging the basalt layer, water table boundary, and potential groundwater migration pathways, integrating results from field studies performed from 2008-2011. Seismic data were used primarily to identify the depth to the basalt layer and the character of the basalt (i.e., weathered, fractured). The 2D ERT and TEM 1D soundings were used to identify additional subsurface contrasts in resistivity and the location of the water table. Interpretations were made from each geophysical method and the known geology and then cross-correlated with each other for a final interpretation. Boundaries for the water table, upper and lower Hanford horizons, and the Hanford-basalt contact were identified as shown in Figure 4.4.

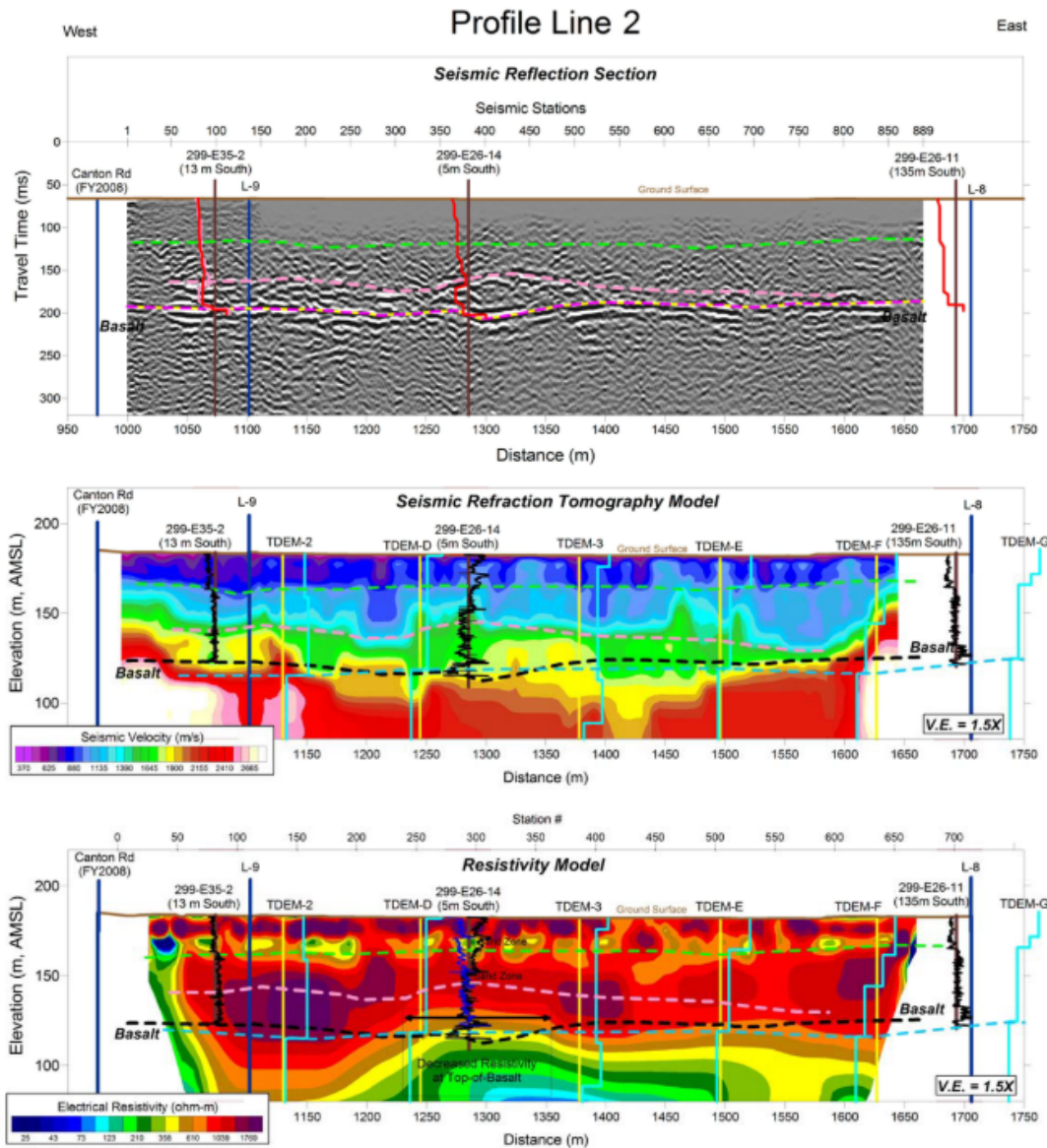


Figure 4.4. Profile Line 2 was collected along a west-to-east profile north of the LERF basins. The interpreted basalt boundary is shown as dashed dark pink (top) and black (middle, bottom) lines. The Hanford formation is separated into two horizons, an upper (dashed green line) and lower (dashed pink line) (Figure 5, Ch2MHill 2012).

Deep (> 500 ft) shear velocity profiling using SASW was performed in the 200 East Area (Lin 2007) and also across the Hanford Site (Stokoe et al. 2014). While the purposes were to assess seismic class and probabilistic rating in the event of an earthquake, the 1D profiles may also be used to map lithologic boundaries.

### **4.3 Electrical Resistivity Tomography**

In the 300 Area, uranium transport (originating from the discharge of waste fluids from two infiltration ponds and a disposal trench) is dependent upon river and groundwater chemistry and fluctuations in the Columbia River stage. The contact between the Hanford formation and the Ringold Formation (the H-R contact) represents a boundary that limits the vertical migration of contaminants. Hanford formation sediment incised into the Ringold Formation enhances the interaction between surface water and groundwater. Therefore, identification of the paleochannels relative to river stage is key to identifying predominant uranium transport pathways.

Slater et al. (2010) conducted continuous waterborne electrical imaging in conjunction with fiber-optic distributed temperature sensor monitoring. They found that seasonal temperature anomalies were correlated with lithology and these were areas in the electrical imaging where the Hanford sediments were thickest and the H-C contact was deepest (Figure 4.5). They determined that these focused areas of exchange play an important role in regulating surface water-groundwater exchange at the 300 Area.

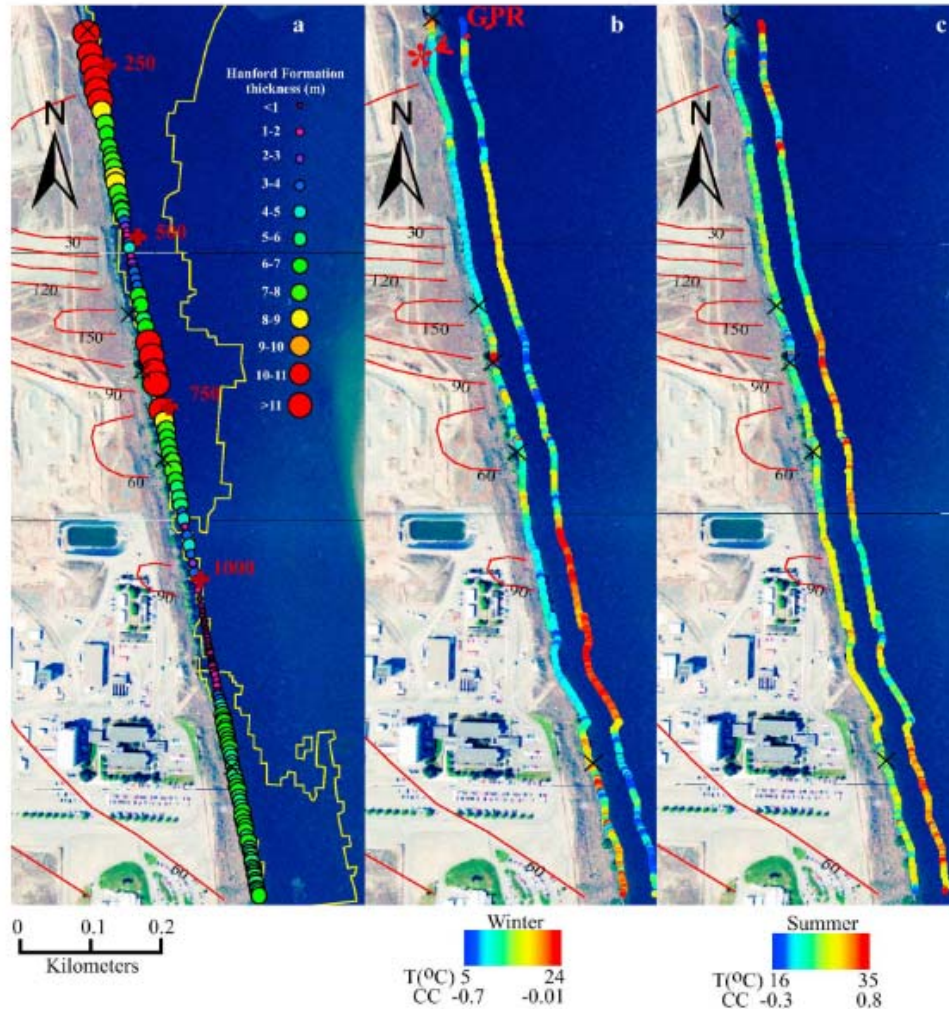


Figure 4.5. a) Hanford formation thickness estimated from waterborne electrical imaging. Low stage temperature measurements collected on b) 3/31/2009 and c) 8/2/2009. Red contours represent uranium concentrations (Slater et al. 2010, Figure 8).

Subsequent time-lapse ERT studies were performed to better define the surface water-groundwater exchange by locating paleochannels along the river corridor. The contrast in specific conductance between the Columbia River water (0.015-0.020 S/m) and the groundwater (0.040-0.045 S/m) enables ERT to detect in 4D when sediments are saturated with river or groundwater (Johnson et al. 2012). A near-shore 3D array was positioned parallel to the riverbank which consisted of four lines of 30 electrodes, spaced at 5 m along each line (total of 120 electrodes). This location straddled the region of focused exchanged identified by Slater et al. (2010). A time-series and time-frequency analysis of the 3D data (Johnson et al. 2012) focused on the dynamics of this exchange in relation to upstream daily dam operations. Segments in time-frequency space identified when surface-water groundwater interactions were most active.

Inland dynamics of the surface water-groundwater exchange in the 300 Area was studied by Wallin et al. (2013) using 2D surface ERT. The array consisted of using 3-2D ERT lines, with two lines containing 60 electrodes spaced at 4 m along the line and one line containing 64 electrodes, spaced at 3 m along the line. Groundwater depths were continuously monitored. The time-lapse 2D ERT analysis consisted of

incorporating a fluctuating water table boundary in a 2D ERT inversion analysis, enabling imaging of both preferential and low permeability zones that created fast flow paths for river water to flow in and out of the aquifer.

Following the work of Wallin et al. (2013), a larger electrode array was installed in the 300 Area to capture larger scale spatiotemporal dynamics (Johnson et al. 2015) (Figure 4.6). The array consisted of 11 electrode lines spacing 25 m apart, each line having 32 electrodes at 10 m spacing, for a total of 352 electrodes. Critical to the interpretation was the incorporation of water table fluctuations and allowing the numerical modeling to only choose models where there was a physically realistic increase in electrical conductivity. The imaging delineated a series of paleochannels that were consistent with the hydrogeological structure inferred from boreholes.

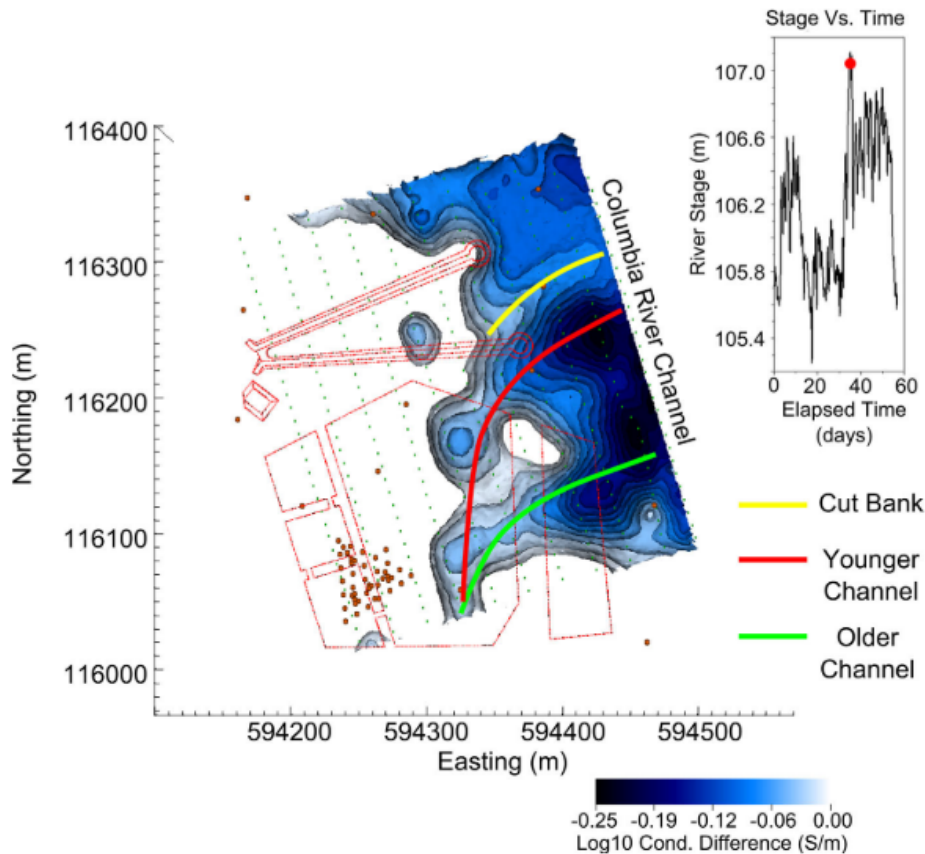


Figure 4.6. Plan view ERT image of high stage river water intrusion within the saturated zone. The colored isosurfaces contour the negative changes in EC with respect to baseline conditions, indicating the presence of river water. River water intrusion flows preferentially through two features interpreted as high permeability paleochannels (Johnson et al. 2015, Figure 11b).

#### 4.4 Ground Penetrating Radar

GPR has not been used specifically to identify paleochannels. However, case studies at the Hanford Site report stratigraphic features could be resolved if data were collected at a resolution-appropriate frequency. The literature reviewed suggests that the lowest frequency allowed to be used on the Hanford Site was 100 MHz (Rucker et al. 2007). Interpretation depths for this frequency are approximately 10 to 12 m, which is not deep enough to resolve paleochannel features at depth.

GPR has been used to reconstruct depositional environments and determine the nature of sedimentary processes because primary reflections usually parallel primary depositional structure (Neal 2004). GPR has been used to identify stratigraphy in sand dunes (Carling et al. 2016; Harari 1996), determine sediment thickness in coves around a lake (Banks and Johnson 2011), and identify major sedimentary structures in a deltaic sedimentary environment (Jol and Smith 1991). The depth of investigations were less than 50 m; however, lower frequency antennae could potentially resolve deeper features in the subsurface. For example, Smith and Jol (1995) found that the maximum probable penetration depths in Quaternary sediments was 52 m (gravel facies) for a 25-MHz antennae and estimated to be 66 m for 12.5-MHz antennae.

At Hanford, GPR has been used to locate metal objects that could interfere with an electrical resistivity survey (Rucker et al. 2007; Myers et al. 2009). GPR is commonly used in this capacity. Other surveys have identified subsurface disturbances (Bergstrom et al., 1993), located clastic dykes, and identified the spatial variability in water content (Knight et al. 2003; Knight et al. 2007).

Table 4.1. Previous geophysical methods used to investigate paleochannels at Hanford.

Site/Location	Date(s) of Survey	Geophysical Technology	Survey Objectives	Reference document	Author(s)	Publication Date
<b>200 Area</b>						
North 200 East Area	Late May-Early June 2009	Seismic Reflection / Vertical profile (check shot)	Seismic landstreamer survey to map depth to the basalt layer and preferential flow paths associated with the basalt surface (referenced in SGW-48478)	SGW-43746	Ch2MHill	Nov-09
North 200 East Area / Gable Gap	FY2010, FY2009, FY2008, FY1979, FY1980	Seismic Reflection / Vertical profile (check shot)	Interpretation and integration of previously acquired seismic data in the Gable Gap using available geologic data to refine the conceptual site model	SGW-48478	Ch2MHill	Apr-11
North 200 East Area near the Liquid Effluent Retention Facility (LERF)	FY2008, FY2011	TEM, 2D ERT Seismic Reflection / Vertical profile (check shot)	Determine the basalt surface and the nature of the sediment-basalt interface beneath the Liquid Effluent Retention Facility to locate RCRA compliance wells	SGW-52467 SGW-52161	Ch2MHill Golder Associates	2012
East of the 200 East Area	Sept 8-12,2004	Seismic surface SASW	Deep (> 500 ft) shear velocity profiling for characterization of soil deposits and rock formations for seismic hazard rating	Lin 2007	Y.Lin	2007
<b>300 Area</b>						
Adjacent to Columbia River	2008	Waterborne ERT	Characterization of surface-water ground-water exchange		Slater	2010
Adjacent to Columbia River	2010	3D ERT	Characterization of surface-water ground-water exchange		Johnson	2012
Adjacent to Columbia River	2011	2D ERT	Characterization of surface-water ground-water exchange		Wallin	2013
Adjacent to Columbia River	2013	3D ERT	Characterization of surface-water ground-water exchange		Johnson	2014
<b>600 Area</b>						
600 Area (200-PO-1 GOU)	6/19-6/20/2008	TEM, Magnetics	Map layers to 150 m depth, detect paleochannels, locate structural breaks	08027	Fluor Hanford Inc.	Sep-08
600 Area (200-PO-1 GOU)	6/29-7/1/2008	FEM, Magnetics	Map upper layers to 50 m depth, detect paleochannels, locate structural breaks	08027R	Fluor Hanford Inc.	Sep-08
600 Area (200-PO-1 GOU)	6/19-6/20/2008 6/29-7/1/2008	TEM/FEM, Magnetics	Evaluation of Phase I Geophysical Technologies in the 200-PO-1 Operable Unit	SGW-38941	Cummins	Sep-08
600 Area (200-PO-1 GOU)	6/19-6/20/2008 6/29-7/1/2008	TEM/FEM, Magnetics	Interpretation of Airborne Electromagnetic and Magnetic Data in the 600 Area	SGW-47839	Ch2MHill	Sep-10
600 Area (North of 300 Area)	2010	FEM, 2D ERT	Testing Ground Based Geophysical Techniques To Refine Electromagnetic Surveys North Of The 300 Area, Hanford, Washington	SGW-47996, Hyde et al., 2009	Ch2MHill, Hyde et al., 2009	Nov-09 Dec-10
<b>Site-wide</b>						
100 B/C, 200 areas, 200-PO-1 GOU, Gable Gap	FY2007, FY2008, FY2009, FY2010	Seismic vertical profile (check shot)	Measurement of Seismic Velocities in 29 Wells at the Hanford Site Seismic Velocities in 29 Wells at the Hanford Site (referenced in SGW-48478)	SGW-47535	Ch2MHill	2010
Site-wide	2013	Seismic Surface SASW	Deep (> 500 ft) shear velocity profiles at each test site	DCN:GR14-1	Stokoe et al., 2014	2014

## 4.5 Conclusions / Recommendations of Previous Work

At the Hanford Site, large scale EM, seismic, and ERT surveys have been designed and executed at scales relevant to delineating large-scale paleochannels. Initial surveys were further verified by performing multiple field campaigns, applying more than one geophysical method, and looking at non-geophysical datasets, such as borehole geologic information.

Discontinuities (i.e., facies changes) have been reported in several studies within the Ringold Formation. The airborne EM (HeliGEOEM and RESOLVE), and ground-based EM-34 and 2D ERT surveys all reported a discontinuity in the low-resistivity sediments, which were assumed to be coarser-grained, Hanford sediments incised into the finer-grained sediments of the Ringold Lower Mud. This boundary is located near the water table and appears to channel groundwater flow. Therefore, geophysical data from surrounding units can also contribute to stratigraphic identification.

The ERT analyses performed in the 300 Area Hanford studies to identify surface-water groundwater interaction (Slater et al. 2010; Wallin et al. 2013; Johnson et al. 2012; Johnson et al. 2015) clearly demonstrate time-lapse ERT as a viable option to image transient processes controlled by stratigraphy in the top 50 m. While static surface ERT has also shown promise to image stratigraphy (Figure 4.2, Figure 4.4), the contrast in resistivity between the contacts can be small (Ch2MHill 2010), underscoring the need to supplement its use with other field data (e.g., borehole sampling, other geophysical surveys). A joint inversion of ERT with other field datasets better constrain the solution (Johnson, et al. 2017; Zhu et al. *Submitted*).

Based on the review of geophysical surveys at Hanford, the following actions are recommended:

- Re-evaluate existing EM survey data where paleochannels were identified using 2D and/or 3D inverse modeling.

Previous airborne EM surveys are of high quality and were collected over multiple frequencies and time windows to have a sensitivity from the very shallow to at least 150 m depth. However, this data has not been inverted to estimate true depths. The depths reported from the EM surveys represented the location where the strongest EM signal were generated as the signal decayed within the subsurface. True depths can only be determined using 2D or 3D inverse modeling, where the data fits the response for a given model of the same dimension. A 2D and/or 3D EM inversion of the RESOLVE (Fluor Hanford Inc. 2008b) and/or HeliGEOEM (Fluor Hanford Inc. 2008a) data can be performed to identify the depths associated with high and low conductivity zones.

Inversions of a shallower depth of investigation EM-34 survey (Ch2MHill 2010) can be compared to the airborne inversions. This EM-34 dataset was never inverted; rather, the 1D-subjective goodness-of-fit analysis matched the observed response to a theoretical response for a given number of layers. To create 2D geoelectrical sections, each 1D layer approximation was interpolated to create 2D geoelectrical sections. Inverting these data could further verify the stratigraphic interpretation of data from the airborne surveys.

- Re-evaluate existing seismic data where basalt and suprabasalt units were identified using inverse modeling.

The previous seismic surveys performed at Hanford were evaluated for reflector locations and geologic contacts were based on borehole check-shot information. Beyond reflection information, the amplitude of the returned wave at an interface is controlled by the contrast in impedance, which is dependent on the bulk density and sonic velocity within the subsurface (Barclay et al. 2008). Seismic reflectivity inversion extracts additional information from seismic data and “facilitates the

interpretation of meaningful geological and petrophysical boundaries in the surface” (Veeken and Silva 2004). The distribution of density and velocity can further inform the conceptual model for the major stratigraphic units.

- Utilize low frequency GPR to image stratigraphy in the top 100 m. Low frequency antennae have not previously been permitted at Hanford. However, a small-scale proof-of-principle effort can be executed to determine the potential feasibility of using GPR for stratigraphic identification.
- Utilize modeling to determine if ERT can be used to characterize paleochannels at other locations across the Hanford Site, which can also include re-evaluating previously collected datasets. This is a cost-effective approach since the feasibility is assessed before a survey is executed in the field.

Only the final action recommended above has been executed and documented in this report. Results of the potential to use ERT for stratigraphic identification are presented in Section 5.0.

## 5.0 Evaluation of Electrical Resistivity Tomography

The potential for an ERT survey to identify a conductive paleochannel between 200 West and 200 East Areas was performed by using a groundwater flow and transport model to provide information on porosity and saturation that are converted to states of bulk electrical conductivity. ERT modeling then simulates the transfer resistance data to image the subsurface and compares the result to the groundwater model (Johnson et al. 2017; Robinson et al. 2019; Vanderborght et al. 2005). The groundwater model utilized the Hanford geologic framework model (Ch2MHill 2016) for the area between 200 East and West shown in Figure 5.1. The Hanford formation has been removed from this figure to highlight incisions of lower elevation into the lower units that may be representative of zones of high transmissivity.

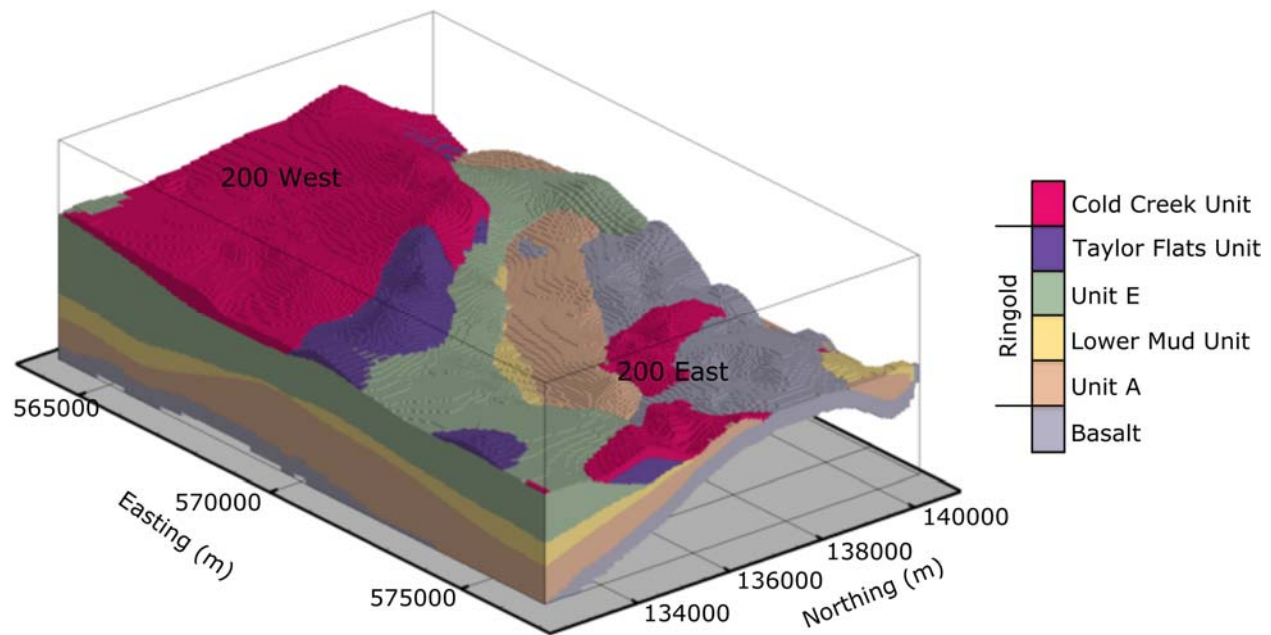


Figure 5.1. The geologic framework model between 200 East and West on the Central Plateau. The Hanford formation has been removed to demonstrate the general shape of a paleochannel between 200 East and West as inferred by areas of lower elevation.

Using simulations to evaluate the likely performance of a field ERT campaign has the following benefits:

- Realistic expectations of information that ERT can provide under the given field conditions and existence of subsurface structures.
- Optimization of ERT design such as electrode spacing and measurement sequence and configuration.
- Identification of potential limitations and constraints.

In this report, the initial state is referred to as the background. Initial simulations indicated that a conductive tracer was needed to so that time-dependent conductivities could be imaged relative to background. Subtracting the background ERT image from the time-lapse removes the static effects of lithology and reveals only what has changed over time, namely the change in bulk conductivity caused by the migration of the tracer. This method is commonly referred to as time-lapse ERT difference imaging and enables the imaging of conductive, ionic tracers travelling through preferential flow pathways.

Simulations were executed to identify a potential transmissive paleochannel ~70 m below the surface in the unconfined aquifer using hypothetical surface ERT arrays. The results represent an initial evaluation of the potential effectiveness of a large-scale ERT field deployment for imaging the hydrostratigraphy and tracer transport between 200 East and West.

## 5.1 Site Description

The simulation domain includes the inferred spatial extents of the paleochannel based on the geologic framework model, and proximity to two candidate tracer injection wells (Figure 5.2). The first candidate injection well is an existing well (699-49-69) with a screened interval at the water table. This well is currently in use as an injection well for the 200-ZP-1 OU carbon tetrachloride pump-and-treat system. The second candidate injection well has been identified as a potential monitoring pump well for fiscal year 2021 (designation MW-10A). The MW-10A location is presumed to be within the paleochannel between the 200 East and West Areas. The planned midpoint screened interval elevation is 106 m, which is within the Ringold Unit A (refer to Figure 5.1). While this planned screened elevation is below the paleochannel according to the geologic framework model, the screened interval is assumed to be completed within the Hanford sediments to represent the paleochannel.

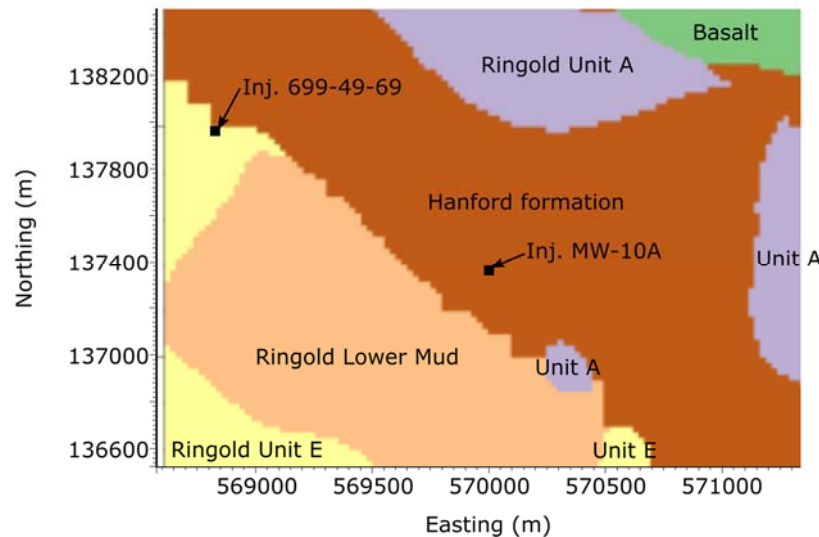


Figure 5.2. Geologic framework model at an elevation of 120 m in the saturated zone. The ERT simulations focus on depths at or below this elevation.

Domain extents are 1400 m in the northing direction and 2300 m in the easting direction, representing an area of 3.22 km<sup>2</sup> (Figure 5.3). Ground surface elevations range from 176.70 to 228.80 m and generally slope downward to the northeast. The water table surface generally slopes eastward from 200 West to 200 East Area, with water table elevations ranging from 129.73 to 121.95 m.

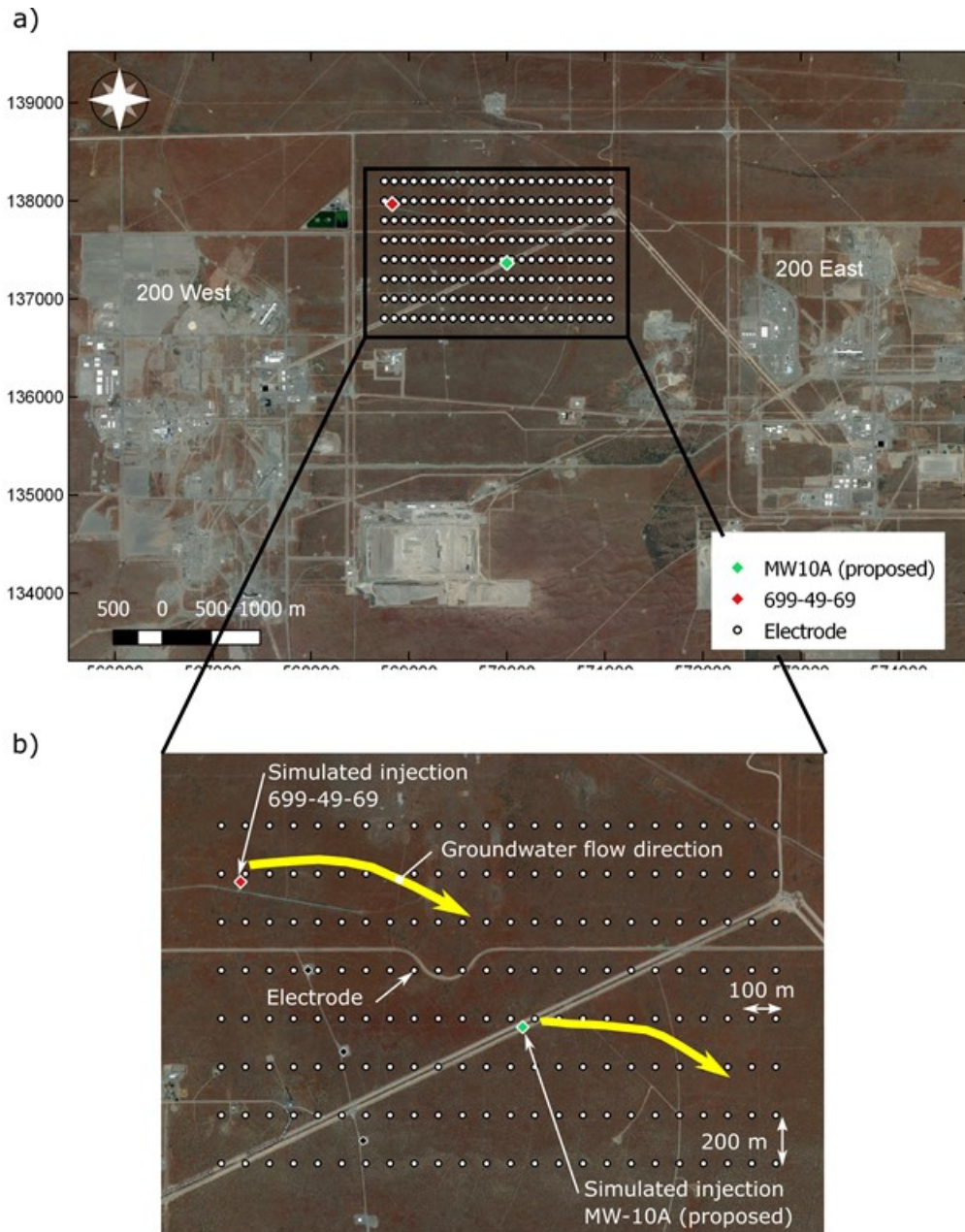


Figure 5.3. a) Potential electrode placement and injection well locations; and b) magnified site view with groundwater flow directions with yellow arrows.

## 5.2 Simulation Details

Simulations of groundwater flow and solute transport were performed using the water operational mode of eSTOMP (Fang et al. 2015), a parallel version of STOMP (White and Oostrom 2006). ERT imaging simulations were conducted using E4D (Johnson 2014; Johnson et al. 2010), an open source 3D modeling and inversion code designed to run on distributed memory parallel computing systems.

The eSTOMP simulator uses a 3D structured grid with orthogonal, hexahedral grid blocks while E4D discretizes the model space with a 3D unstructured tetrahedral mesh. Therefore, eSTOMP output was

interpolated to the E4D mesh. The mesh interpolation code of Johnson et al. (2017) was adapted so that each E4D element is divided into sub-elements and a tri-linear interpolation is used to determine the weighting from eSTOMP output. This integrated approach minimizes discretization differences.

### 5.2.1 Flow and Transport

The tops of major hydrostratigraphic units at the site were defined from borehole geologic and geophysical data (Hammond and Lupton 2015). Surfaces defining these tops were used to define the spatial distribution of lithological types for the eSTOMP-based 3D numerical flow and transport model. The 3D model represents a 4-km by 4-km area in between the 200 East and West Areas. The vertical extent of the model covers an elevation range from 38 to 234 m, from basalt to ground surface. Hydraulic conductivity, porosity, and density for the hydrostratigraphic units defined in the flow and transport model are shown in Table 5.1 (Rockhold et al. 2018; Budge 2017). The model was discretized using 2.0 million grid blocks. Since the topography over the area is variable, grid blocks lying above the elevation of the ground surface are defined as inactive (non-computational). Uniform 25-m grid spacing was used in the horizontal direction and uniform 2-m grid spacing was used in the vertical direction.

Lateral boundaries for groundwater flow were defined using seepage face boundary conditions in which base pressures and gradients along segments of the lateral boundaries were defined by interpolating data from a database of water table elevations for a Hanford Site-wide well monitoring network. Historical water level data from 1944-2016 were used. Boundary conditions for times later than 2016 were held constant at the last values used for 2016. The upper recharge boundary conditions were defined based on a recharge map for the site (Fayer and Walters 1995). Lateral boundaries for transport were defined as outflow type boundary conditions. The upper boundary condition for transport was defined as a zero-flux condition.

Beginning in 2020, a tracer injection of 100,000 gallons was simulated at two borehole locations: 699-49-69 and MW-10A, over a period of 7 days just below the water table. The tracer concentration used in the modeling was 60 g/L KBr. Given this high concentration, density effects were accounted for in the eSTOMP transport modeling. The addition of a conductive tracer can create sharp concentration boundaries with the native groundwater. To account for these sharp boundaries, a total variation diminishing transport scheme was used to ensure mass conservation without numerical dispersion. The eSTOMP output parameters used for the ERT simulations were saturation, porosity, and tracer concentration.

Table 5.1. Input parameters for flow and transport model simulations.

	Density (kg/m <sup>3</sup> )	Porosity	Hydraulic Conductivity (m/day)	
			X-Y Direction	Z Direction
Basalt	2710	0.100	1.40E-05	1.40E-05
Ringold Unit A	2864	0.221	1.00E+00	1.00E-01
Ringold lower mud unit	2710	0.400	8.00E-03	8.00E-04
Ringold Unit E	2864	0.221	4.36E+00	4.30E-01
Ringold Taylor Flats unit	2723	0.391	2.00E+00	2.00E-01
Cold Creek Unit	2709	0.250	2.00E+03	1.00E+02
Hanford formation	2620	0.250	6.14E+01	3.80E+00

## 5.2.2 Petrophysical Transform

eSTOMP outputs parameters of interconnected porosity  $\phi_{int}$  and aqueous saturation  $S$  and tracer concentrations that are transformed into bulk electrical conductivity  $\sigma$  for the ERT simulations. For a partially saturated electrically resistive sediment, Archie's law (Archie 1942) describes the relationship between  $\sigma$  and pore space properties as

$$\sigma = \sigma_w \phi_{int}^m S^n \quad (5.1)$$

Note that surface conduction is neglected in Eq. (5.1), which is valid to a first-order, given that the target zones are permeable buried features with coarser sediments. However, further work needs to be performed on finer sediments, particularly those in the Ringold and Cold Creek units to validate this assumption. The cementation exponent  $m$  is a function of the rate of change in pore complexity with porosity (Yue 2019), dependent on particle shape and orientation (Niu and Zhang 2018) and typically varies between 1.2 and 4.4 (Lesmes and Friedman 2005). In this assessment, a value of 1.8 was used because it is considered representative of consolidated sandstones at Hanford (Archie 1942; Lesmes and Friedman 2005). The saturation exponent  $n$  is associated with the additional tortuosity due to the replacement of pore fluid with air (an insulator). Commonly,  $n = 2$  is used and was also assumed in this assessment (e.g. Brunet et al. 2010; Day-Lewis et al. 2005).

Fluid conductivity  $\sigma_w$  is the summation of the background groundwater conductivity and the contribution from the tracer. Groundwater samples between 200 East and West have an average  $\sigma_w$  equal to 0.05 S/m (see Section 5.2.4). The assumed composition of the ionic tracer was potassium bromide (KBr). Isono (1984) identified the relationship between KBr concentration and fluid conductivity as shown in Figure 5.4. A concentration of 60 g/L of KBr was assumed to maximize conductivity contrasts ( $\sigma_w$  of 4.764 S/m) while maintaining a realistic amount of KBr to be injected into the aquifer.

Feasibility of ERT for a deep target is sensitive to the vadose zone conductivity parameter. Inversion of surface electrical resistivity data from the Hanford B-Complex in the 200 East Area by Johnson and Wellman (2013) suggest a range in vadose zone conductivities from  $10^{-3}$  to  $10^{-3.5}$  S/m. In contrast, the flow and transport model developed for this feasibility evaluation suggests vadose zone conductivities are an order of magnitude lower. A lower vadose zone conductivity will result in a deeper current penetration during an ERT survey. Given that the region of interest was at the depth of the water table, a lower conductivity would be more favorable in the ERT simulations. To maintain the distribution of saturation and porosity predicted by the flow and transport modeling while also using a more conservative approach (e.g., depth penetration of current would likely be shallower with a more resistive vadose zone and therefore less favorable for ERT imaging), this study scaled the vadose zone conductivities by the bounds defined by the inversion of surface data at the B-Complex (Johnson and Wellman 2013).

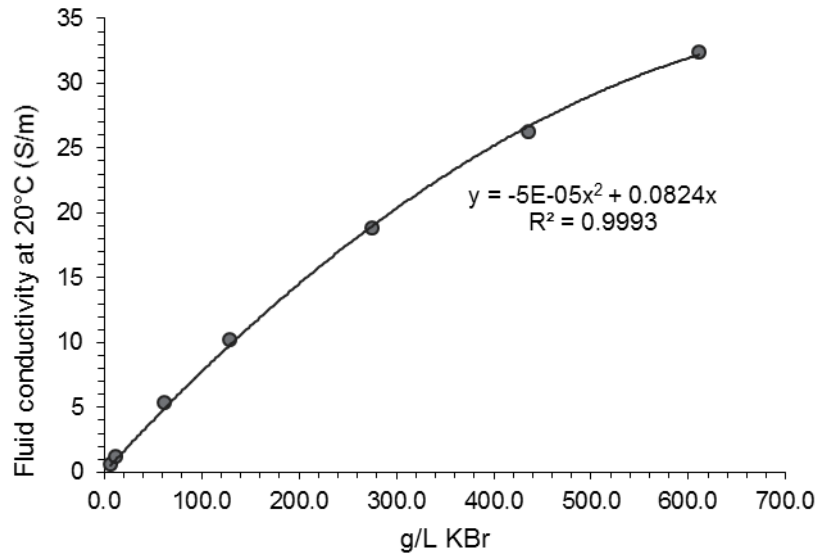


Figure 5.4. The relationship between potassium bromide (KBr) concentration and fluid conductivity (from Isono 1984).

### 5.2.3 Electrical Resistivity Tomography

The unstructured tetrahedral mesh used in the ERT modeling contained 1.4 million elements. Surface topography was incorporated at 50-m resolution, and from this information, nearest neighbor elevations were used for electrode elevations. The water table represented a sharp electrical conductivity contrast and was explicitly incorporated in the mesh as a variable elevation surface using the same water level measurements as in the flow and transport modeling. Since the region of interest was below the water table, finer tetrahedral elements were used below this boundary to an elevation of 0 m. The ERT modeling solved for conductivity within each tetrahedral element. Therefore, finer elements increased the ability of the model to solve for spatial variability within the region of interest.

A surface grid of 192 electrodes was simulated with dimensions of 24 x 8 electrodes (Figure 5.2). In the easting direction, there was a 100-m separation; in the northing direction, there was a 200-m separation. The total surface area of the electrode grid was 3.22 km<sup>2</sup> (2.3 m x 1.2 m). The hypothetical ERT survey consisted of 2828 four-electrode measurements in a 3D configuration. The configuration used was such that the current injection was between two electrodes in a row or columns and potential measurements were along the column (if current injection was within the same row) or row (if current injection was within the same column) of the injection electrodes. This design resulted in capturing lateral variations relative to a standard dipole-dipole survey that places electrical current electrodes adjacent to the potential electrodes. Noise levels were assumed to be 2% with an absolute error of 0.001 ohms, which is based on previous studies in the 300 Area (Johnson and Wellman 2013).

Before the tracer injection was simulated, a background dataset was inverted to determine if the conductivity structure could delineate lithologic boundaries (refer to Figure 5.1) at the water table elevation. A constraint was added in the background modeling that favored higher conductivities in the saturated zone than in the vadose zone. This provides the inversion with realistic physical information and is enforced only if the data can fit such a constraint. Other constraints used were nearest neighbor smoothing between adjacent elements in the vadose and saturated zones.

Time-lapse ERT simulations began after the tracer injections and used the background conductivity as the starting model. Changes from the background model were inverted within the finely discretized region below the water table. This assumes there were no site activities that would produce changes in conductivity within the vadose zone that would affect the saturated zone, which is justified at this scale assuming annual recharge remains relatively constant (Oostrom et al. 2017). Decreases in conductivity were penalized, subject to data fit, which assumed conductivity remains constant or increases over time within the monitoring zone below the water table and over the simulation period. This focuses the inversion on changes within the saturated zone due to addition of the tracer. Time-lapse simulations solved for a smooth conductivity distribution, in space and time relative to the background model.

#### 5.2.4 Other Modeling Considerations

Nitrate is an inorganic dissolved solid that carries a negative ionic charge and therefore increases fluid conductivity. Nitrate is present throughout the Hanford Central Plateau. Since ERT cannot distinguish between ionic sources, nitrate in large concentrations could mimic the response from an injected tracer. While this would not necessarily be detrimental to paleochannel identification (i.e. presumably nitrate would also preferentially flow within the paleochannel), the impact of nitrate within the groundwater needs to be quantified. Between 200 East and West, there are no known persistent source locations leaching nitrate, therefore historical records were used to determine existing concentrations.

Nitrate concentrations have been measured for decades and are available through the Hanford Environmental Information System (HEIS) which can be accessed via PHOENIX (<https://phoenix.pnnl.gov>). Fluid specific conductance is also routinely determined from collected groundwater samples. It was assumed that nitrate is correlated with fluid specific conductance, more than any other constituent in the groundwater, and therefore could act as a marker of nitrate concentrations (Oostrom et al. 2017). For co-located sample ID and dates, nitrate and fluid specific conductance were retrieved for all wells between 200 East and West Areas. Thirty-four unique well locations were identified in this area and a total of 667 total records were retrieved over the date range 12/12/1983-11/2/2018. The coefficient of determination ( $R^2$ ) of fluid specific conductance versus nitrate concentration was equal to 0.611 (Figure 5.5). Therefore, a first-order linear fluid specific conductance relation could be used as a proxy for nitrate concentrations. The regression equation shown in Figure 5.5 was used to convert simulated tracer concentrations to  $\sigma_w$  in Eq. (5.1).

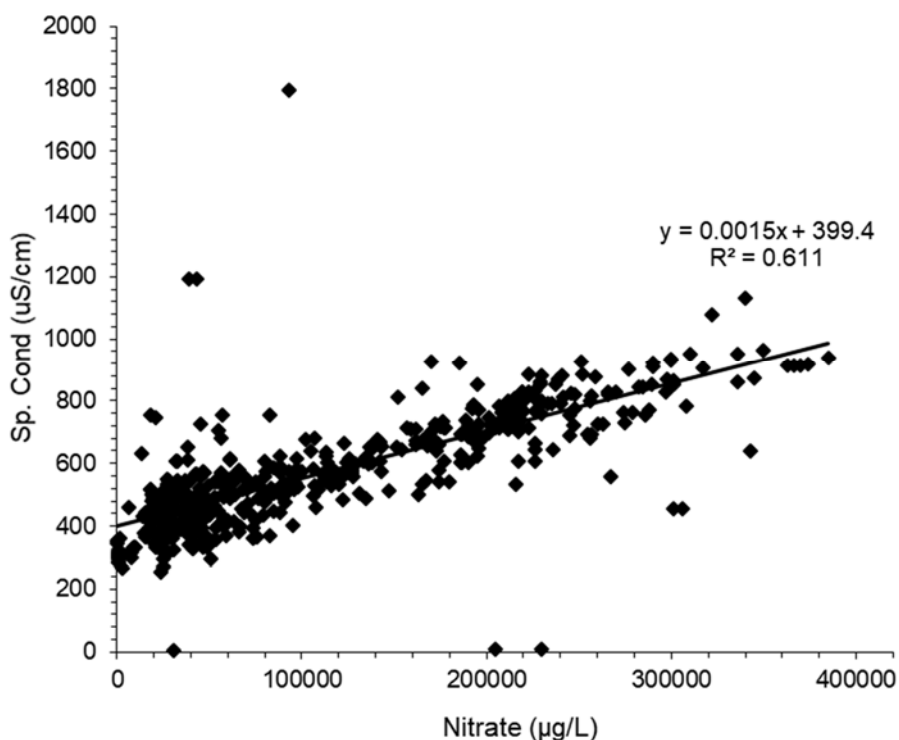


Figure 5.5. A comparison of HEIS nitrate concentrations and fluid specific conductance from boreholes within and surrounding the area between 200 East and West Areas between 12/12/1983 and 11/2/2018.

Average and median specific conductance from the collection of wells between 200 East and West are 0.0552 S/m (std dev=0.0176 S/m) and 0.0516 S/m, respectively. At full strength, the theoretical fluid specific conductance (see Figure 5.4) of the tracer is 4.7 S/m. Dilution of the tracer to 10% of the original value has a theoretical fluid specific conductance (see Figure 5.5) of 0.49 S/m, or one order of magnitude above the fluid specific conductance from nitrate. Therefore, given the low fluid specific conductance due to the presence of nitrate and the lack of persistent nitrate sources in this area, nitrate was not considered or accounted for as a source in the flow and transport modeling.

## 5.3 Results

### 5.3.1 Flow and Transport

The flow and transport results for the tracer injection are shown in Figure 5.6. For both candidate injection wells, minimum lateral spreading occurs during the first few years of simulation (Figure 5.6a-c). By 2025 (Figure 5.6d), more significant lateral spreading occurs near well 699-49-69 in the direction of groundwater flow because the tracer has entered the high permeability paleochannel. By contrast, the tracer injection from MW-10A shows less horizontal spreading and quicker southeasterly flow direction due to its location within the paleochannel. For both wells, the trajectories of the simulated plumes follow the boundary of paleochannel as depicted in the geologic framework model.

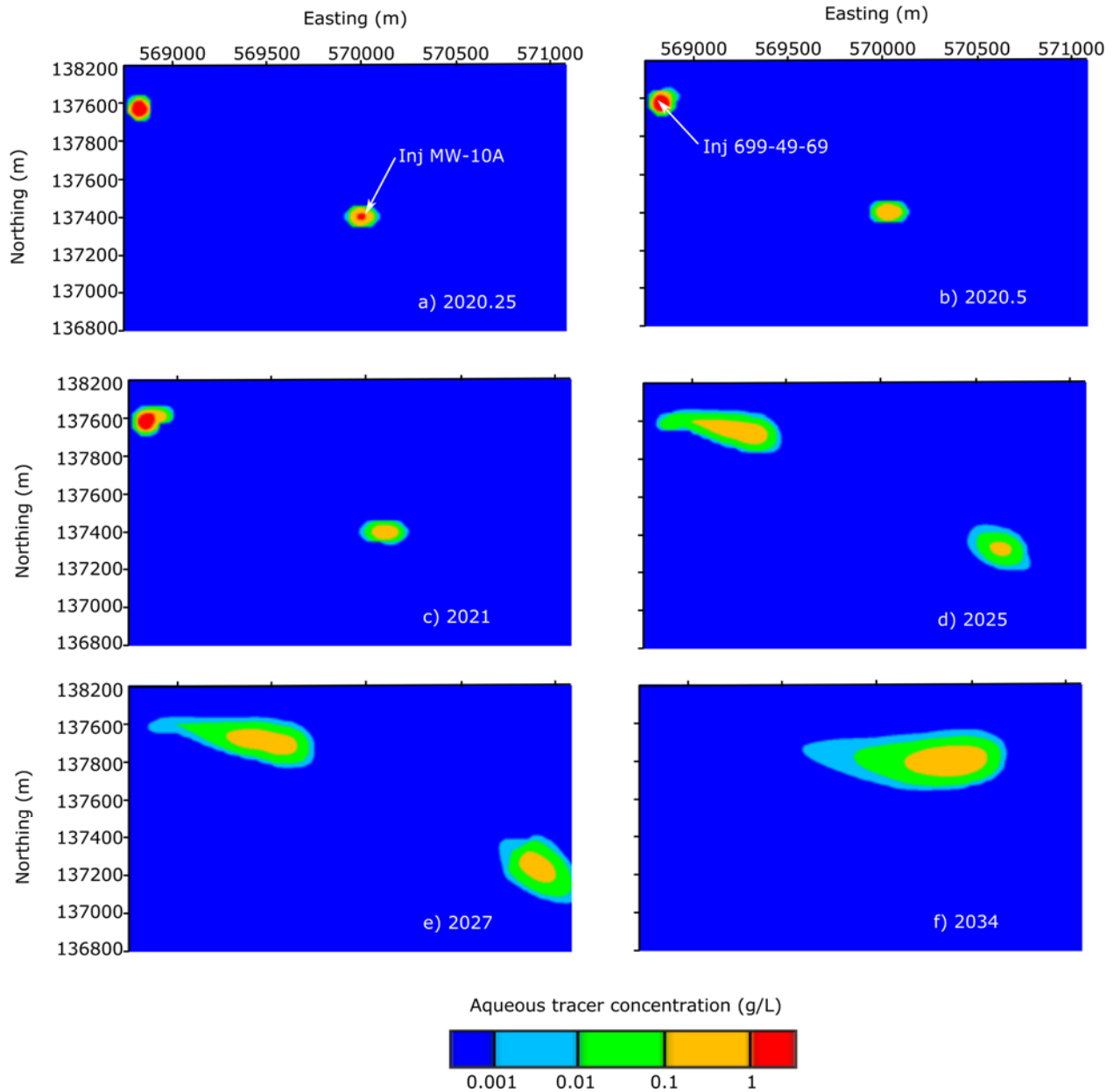


Figure 5.6. Results of flow and transport simulations of a tracer injection into wells 699-49-69 and MW-10A at elevation 120 m. Shown are aqueous concentrations after the tracer injection ceased 2020 a) 2020.25; b) 2020.5; c) 2021; d) 2025; e) 2027; f) 2034.

### 5.3.2 Electrical Resistivity Tomography

The background ERT image is shown alongside the flow and transport  $\sigma$  in Figure 5.7. The left figures (Figure 5.7a-b) are the plan and elevation view of the flow and transport  $\sigma$  and electrodes are shown for reference. The right figures (Figure 5.7c-d) are the inverted ERT images. The color scale for the ERT images have a maximum value that is one order of magnitude lower than for the flow and transport  $\sigma$  to so that the conductivity structure can be observed. In general, the plan views (Figure 5.7a and Figure 5.7c) show a similar structure, although the ERT  $\sigma$  (Figure 5.7c) structure is less resolved. This is especially noticeable near the edges of the electrode grid, where measurement density is lower.

Resolution with depth, from the surface to the basalt is shown in Figure 5.7b and Figure 5.7d for the groundwater model and ERT image, respectively. Using nearest-neighbor smoothness constraints within the water table (~70 m depth), the ERT inversion fit the data to a model with the least amount of structure that can satisfy the data. The ERT image shows limitations in its ability to resolve stratigraphy with depth relative to the stratigraphy represented in the groundwater model (Figure 5.7a and Figure 5.7b). For this electrode configuration, lateral stratigraphy is better resolved than with depth.

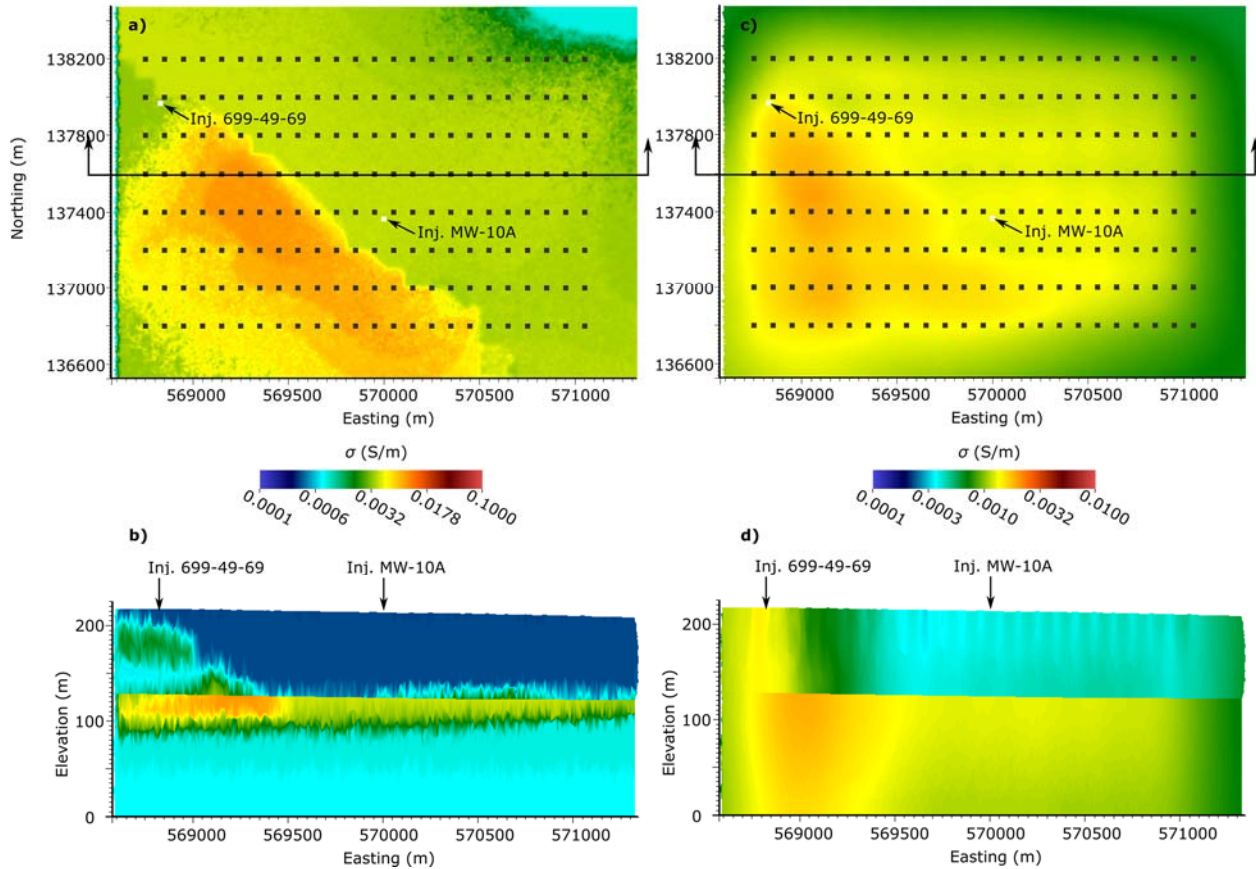


Figure 5.7. Flow and transport  $\sigma$  in plan view a) and elevation view b). Background ERT  $\sigma$  images are shown in plan view c) and elevation view with a 5:1 vertical exaggeration d). Color scales are one order of magnitude lower for the ERT  $\sigma$  relative to the flow and transport model  $\sigma$  to highlight the variability in conductivity structure of the ERT  $\sigma$ , which would otherwise not be visible.

Time-lapse ERT imaging results are compared to the flow and transport  $\sigma$  in Figure 5.8 as logarithmic changes in conductivity relative to background. ERT images are shown as orange-shaded isosurfaces and the flow and transport model  $\sigma$  is shown as blue-shaded isosurfaces. The color scales differ between the two images because ERT image is less resolved than the flow and transport model  $\sigma$ .

Images are shown for select years to represent early and late times in the injection migration. The first result shown is at 2025.25, 3 months after the tracer injections ceased at wells 699-49-69 and MW-10A (Figure 5.8a). While images before this date detected changes in bulk conductivity, 2025.25 is the first image of changes occurring near the injection wells. ERT imaging artifacts are also noted in these images, where ERT identifies changes that do not correspond to the flow and transport model  $\sigma$ . These are more evident in early times but dissipate at later times (Figure 5.8b). The ERT estimated  $\sigma$  overlaps the spatial

extent of the flow and transport  $\sigma$ , and appears as more spatially extensive due to the limited resolution obtained in the inversion modeling.

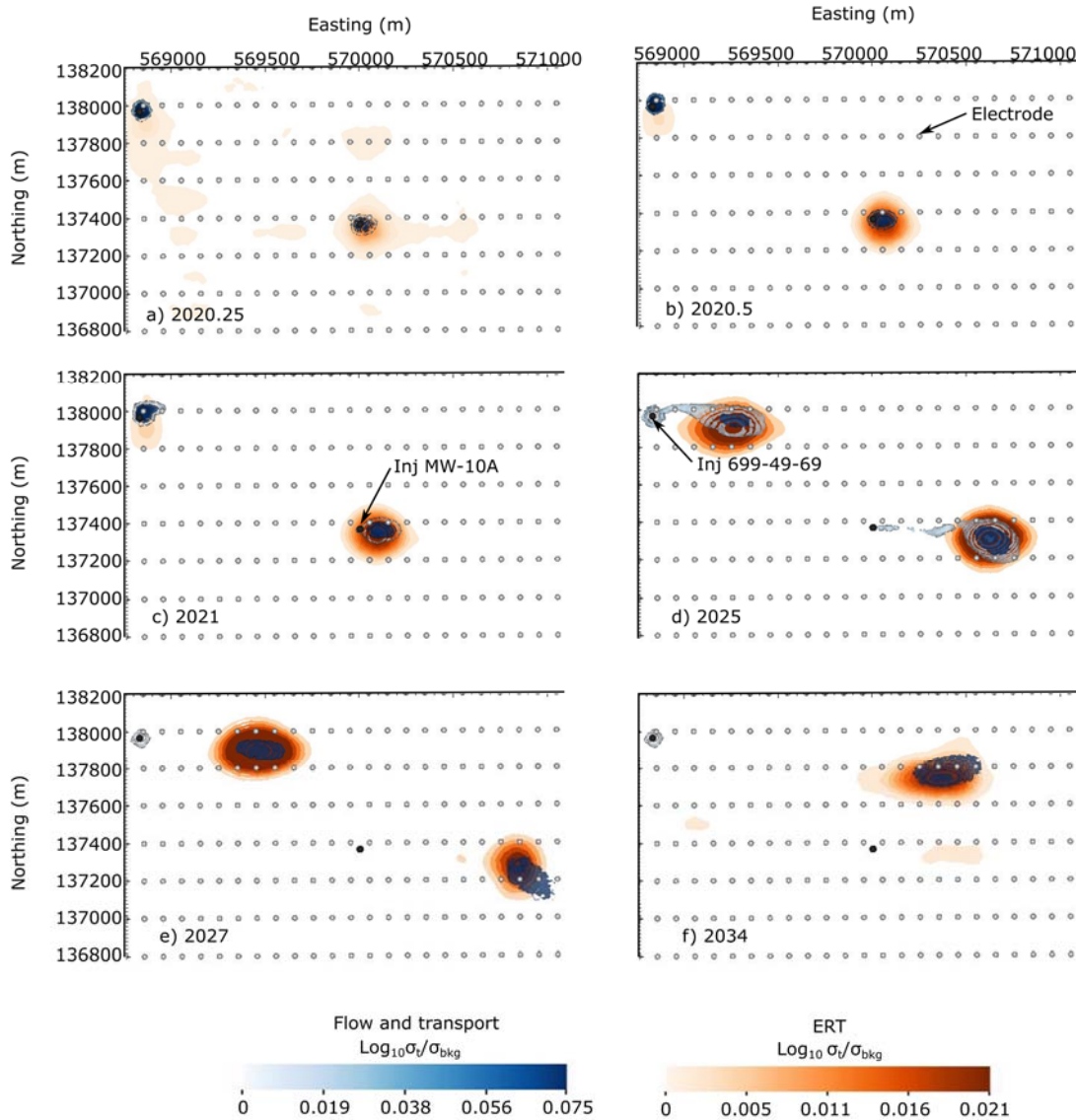


Figure 5.8. Time-lapse ERT  $\sigma$  results alongside flow and transport  $\sigma$  conceptual site models. Both models are represented as isosurfaces of logarithmic change from background (year 2020) values. Simulations results are shown after the tracer injection has ceased at a) 2020.25; b) 2020.5; c) 2021; d) 2025; e) 2027; and f) 2034.

## 5.4 ERT Evaluation Conclusions

Based on a conceptual geologic framework and transient flow and transport model simulations, the 3D surface ERT simulations defined to a limited extent, static conductivity (stratigraphic) structures from a background image (Figure 5.7) and imaged tracer migration from injections in two separate wells using time-lapse imaging (Figure 5.8).

The ERT analysis revealed that 3D surface static imaging can provide limited information on conductivity contrasts related to lithologic boundaries at the depth of interest (~70 m below ground surface). Lateral channel boundaries were imaged relative to the flow and transport model  $\sigma$ . Imaging with depth was less successful suggesting that static ERT imaging can be used to define lateral boundaries but large volumes of water and high tracer concentrations are required.

Field-deployment must consider the assumptions made in the flow and transport and ERT modeling. For example, the geological framework used in the flow and transport simulations depict continuous hydrostratigraphy, and the physical properties within each unit were assumed to be constant. However, hydrostratigraphic units are heterogeneous, with hydraulic properties varying within major stratigraphic units, which may influence the ability of ERT to image major stratigraphic units as defined by the conductivity contrasts provided with the flow and transport model. The cementation  $m$  and saturation  $n$  exponents defined in the Archie transformation [Eq. (5.1)] were assumed to be constant for all units, but identifying formation specific parameters that relate to bulk electrical conductivity can provide more accurate models for ERT simulations.

The imaging results presented in this report represent a single geologic conceptualization of the paleochannel and its surrounding units. Additional geologic conceptual models and parameterizations should be investigated to identify the potential for alternative outcomes. For example, the potential for hydraulic gradients to divert flow around the paleochannel needs to be evaluated as part of the ERT assessment. This ERT imaging depicts results for a tracer with a target concentration and volume. A range of tracer concentrations and volumes needs to be evaluated to minimize these quantities while still imaging the paleochannel.

While this analysis focuses on evaluating the usefulness of an ERT survey before field operations commence, information from ERT surveys can also be used to inform and update flow and transport models. Conversely, flow and transport models can inform ERT feasibility prior to costly field implementation.

## 6.0 Summary and Recommendations

This section summarizes results and provides further recommendations on using geophysical methods to identify and detect transmissive subsurface features or paleochannels. The evaluation in this report was performed by (1) reviewing historical field investigations where the objective of the field campaign was specifically related to identifying transmissive features; and (2) conducting a hydrogeophysical simulation to assess the feasibility of using ERT to characterize transmissive, paleochannel features.

Previous geophysical field surveys at Hanford employed EM, seismic, and ERT methods to delineate subsurface structure and stratigraphy. EM surveys in the 600 Area were conducted to identify transmissive features in the top 100 m of the subsurface. Seismic surveys near Gable Gap and LERF were undertaken to map the depth to the basement basalt and identify lithologic contacts within suprabasalt sediments. ERT has been utilized to map lithologic boundaries and structure in support of other investigations and time-lapse ERT has been used to better understand surface water-groundwater interactions at the 300 Area. Each of these geophysical methods samples a volume of Earth and measures a bulk quantity. Therefore, the success of a method for stratigraphic identification depends on a contrast in biological, chemical, and physical properties that impact the measured quantity and the resolution of the geophysical survey.

Depths for EM and seismic geophysical models were estimated during previous investigations by calibrating to known information, such as EM receiver height and seismic borehole check shots to known units, respectively. However, this localized information for stratigraphic interpretation may not be sufficient for a spatially extensive 3D model. True depth estimates for a 3D model can only be obtained through numerical inverse modeling, which can also use all available information for ground truthing. Existing datasets that have not been previously inverted can be re-evaluated without the expense of conducting an additional field survey.

ERT has a distinct advantage over other geophysical methods in imaging transient processes because sensors (i.e., electrodes) can be left in place. This allows for continuous, autonomous data collection and analysis over time.

The hydrogeophysical simulation represents the first step in a multi-phased evaluation of a large-scale ERT field survey with a tracer injection for paleochannel identification. The simulations showed promising results, but additional site-specific information is warranted to better determine its viability and optimize its design. Appendix A contains a summary of proposed activities that support a more in-depth evaluation. These activities are based on the following:

1. The spacing of electrodes in the simulation is relatively large (100 m along each row and 200 m between each row); therefore, the electrical current injection necessary to achieve high quality measurements needs to be verified. The amount of actual field noise needs to be determined as well as any effects from infrastructure that were not accounted for in the modeling.
2. The time scale of the injected tracer transport monitoring is over a period of years and ERT imaging results may not be visible for at least 3 months. Better estimates of aquifer hydraulic properties are needed to refine these estimates and identify uncertainty bounds on the potential range of tracer behavior and ERT interpretation.
3. Once boundaries for site-specific ERT noise levels and aquifer properties are better determined, these data can be incorporated into models for further evaluation. A bromide tracer concentration

of 60 g/L was used in these simulations, which is noticeably higher than previous groundwater tracer studies performed on the Hanford Site. An ERT numerical sensitivity analysis, which considers a range of injected tracer concentrations can provide likely ERT imaging outcomes for a given concentration / contrast in electrical conductivity. Challenges associated with permitting and approval for tracer injection tests involving high concentrations and volumes will also need to be evaluated further.

These additional assessments are needed to make a more informed decision on the viability of conducting a large-scale tracer test with ERT monitoring for stratigraphic identification.

## 7.0 Quality Assurance

This work was performed in accordance with the Pacific Northwest National Laboratory (PNNL) Nuclear Quality Assurance Program (NQAP). The NQAP complies with the U.S. Department of Energy Order 414.1D, *Quality Assurance*, and 10 CFR 830 Subpart A, *Quality Assurance Requirements*. The NQAP uses NQA-1-2012, *Quality Assurance Requirements for Nuclear Facility Application*, as its consensus standard and NQA-1-2012, Subpart 4.2.1, as the basis for its graded approach to quality.

This work emphasized acquiring new theoretical or experimental knowledge and the initial stages of proving scientific theory. The information associated with this report should not be used as design input or operating parameters without additional qualification. The work scope associated with this report has been graded as *Basic* research.

## 8.0 References

- 10 CFR 830, *Energy/Nuclear Safety Management*. U.S. Code of Federal Regulations.
- Annan AP. 2009. *Electromagnetic Principles of Ground Penetrating Radar*. Vol. 1(1), 1-37.
- Archie GE. 1942. "The Electrical Resistivity Log as an Aid in Determining Some Reservoir Characteristics." *Petroleum Transactions of AIME* 146: 54–62.
- ASME NQA-1-2000, *Quality Assurance Requirements for Nuclear Facility Applications*. American Society of Mechanical Engineers, New York, NY.
- ASTM International. 1999. ASTM D6429-99, *Standard Guide for Selecting Surface Geophysical Methods*. West Conshohocken, PA. [www.astm.org](http://www.astm.org).
- Banks WSL, and CD Johnson. 2011. *Collection, Processing, and Interpretation of Ground-Penetrating Radar Data to Determine Sediment Thickness at Selected Locations in Deep Creek Lake, Garrett County, Maryland, 2007*. Scientific Investigations Report 2011–5223, US Department of the Interior, US Geological Survey, Reston, VA.
- Barclay F, KB Rasmussen, A Cooke, D Cooke, D Salter, D Lowden, S Pickering, A Rasmussen, and R Roberts. 2008. "Seismic Inversion : Reading Between the Lines." *Oilfield Review*, 42–63.
- Beamish D. 2004. "Airborne EM Skin Depths." *Geophysical Prospecting* 52: 439–49.
- Behroozmand A, K Keating, and E Auken. 2014. "A Review of the Principles and Applications of the NMR Technique for Near-Surface Characterization." *Surveys in Geophysics* 36 (1): 27–85. <https://doi.org/10.1007/s10712-014-9304-0>.
- Bergstrom KA, TH Mitchell, and JR Kunk. 1993. *Interpretation of Ground Penetrating Radar Data at the Hanford Site, Richland, Washington*. WHC-SA-2018-FP, Westinghouse Hanford Co., Richland, WA.
- Bevan BW and TN Smekalova. 2013. "Magnetic Exploration of Archaeological Sites." *Good Practice in Archaeological Diagnostics*, 133–52. Springer, Cham. [https://doi.org/10.1007/978-3-319-01784-6\\_7](https://doi.org/10.1007/978-3-319-01784-6_7).
- Blakely RJ. 1996. *Potential Theory in Gravity and Magnetic Applications*. Cambridge University Press.
- Binley A. 2015. "Tools and Techniques: Electrical Methods." *Treatise on Geophysics*, 233–59. <https://doi.org/10.1016/B978-0-444-53802-4.00192-5>.
- Bjornstad BN and DC Lanigan. 2007. *Geologic Descriptions for the Solid-Waste Low Level Burial Grounds*. PNNL-16887, Pacific Northwest National Laboratory, Richland, WA.
- Bjornstad BN, PD Thorne, BA Williams, GV Last, GS Thomas, MD Thompson, JL Ludwig, and DC Lanigan. 2010. *Hydrogeologic Model for the Gable Gap Area , Hanford Site*. PNNL-19702, Pacific Northwest National Laboratory, Richland, WA.
- Brunet P, R Clément, and C Bouvier. 2010. "Monitoring Soil Water Content and Deficit Using Electrical Resistivity Tomography (ERT) – A Case Study in the Cevennes Area, France." *Journal of Hydrology* 380 (1–2): 146–53. <https://doi.org/10.1016/j.jhydrol.2009.10.032>.

Budge TJ. 2017. *Model Package Report: Central Plateau Groundwater Model, Version 8.4.5*. CP-47631, Rev. 4, U.S. Department of Energy, Office of Environmental Management, Washington, D.C.

Carling PA, CS Bristow, and AS Litvinov. 2016. “Ground-Penetrating Radar Stratigraphy and Dynamics of Megaflood Gravel Dunes.” *Journal of the Geological Society* 173 (3): 550–59. <https://doi.org/10.1144/jgs2015-119>.

Ch2MHill. 2016. *Development of the Hanford South Geologic Framework Model, Hanford Site, Washington Fiscal Year 2016 Update*. ECF-HANFORD-13-0029 Rev. 4, CH2M Hill Plateau Remediation Company, Richland, WA.

Ch2MHill 2012. *Integrated Surface Geophysical Investigation Results at Liquid Effluent Retention Facility, 200 East Area, Hanford, Washington*. SGW-52467, CH2M Hill Plateau Remediation Company, Richland, WA.

Ch2MHill. 2011. “Interpretation and Integration of Seismic Data in the Gable Gap.” SGW-48478, CH2M Hill Plateau Remediation Company, Richland, WA.

Ch2MHill. 2010a. *Testing Ground Based Geophysical Techniques to Refine Electromagnetic Surveys North of the 300 Area, Hanford, Washington*. SGW-47996, Rev 0, CH2M Hill Plateau Remediation Company, Richland, WA.

Ch2MHill. 2010b. *Interpretation of Airborne Electromagnetic and Magnetic Data in the 600 Area*. SGW-47839, CH2M Hill Plateau Remediation Company, Richland, WA.

Ch2MHill. 2009. *Landstreamer / Gimbaled GeoPhone Acquisition of High Resolution Seismic Reflection Data North of the 200 Areas - Hanford Site Landstreamer / Gimbaled GeoPhone Acquisition of High Resolution Seismic Reflection Data North of the 200 Areas - Hanford Site*. SGW-43746, CH2M Hill Plateau Remediation Company, Richland, WA.

Dahlin T, and V Leroux. 2012. “Improvement in Time-Domain Induced Polarization Data Quality with Multi-Electrode Systems by Separating Current and Potential Cables.” *Near Surface Geophysics* 10 (6): 545–65. <https://doi.org/10.3997/1873-0604.2012028>.

Day-Lewis FD, K Singha, and AM Binley. 2005. “Applying Petrophysical Models to Radar Travel Time and Electrical Resistivity Tomograms: Resolution-Dependent Limitations.” *Journal of Geophysical Research B: Solid Earth* 110 (8): 1–17. <https://doi.org/10.1029/2004JB003569>.

DOE Order 414.1D, *Quality Assurance*. U.S. Department of Energy, Washington, D.C.

DOE. 2002. *Standardized Stratigraphic Nomenclature for Post-Sediments Within the Central Pasco Basin*. Vol. 39, U.S. Department of Energy, Washington, D.C.

DOE. 2017. *Hanford Site Groundwater Monitoring Report for 2017*. DOE/RL-2017-66, U.S. Department of Energy, Richland Operations Office, Richland, WA.

DOE. 2011. *Hanford Site Groundwater Monitoring for 2011*. DOE/RL-2017-66, U.S. Department of Energy, Richland Operations Office, Richland, WA.

Dyck AV and GF West. 1984. “The Role of Simple Computer Models in Interpretations Wide-Band, Drill-Hole Electromagnetic Surveys in Mineral Exploration.” *Geophysics* 49 (7): 957–80.

- Falzone S, J Robinson, and L Slater. 2018. "Characterization and Monitoring of Porous Media with Electrical Imaging : A Review." *Transport in Porous Media*, 26. <https://doi.org/10.1007/s11242-018-1203-2>.
- Fang YD, D Appriou, DH Bacon, V Freedman, ML Rockhold, C Ruprecht, GD Tartakovsky, MD White, SK White, and F Zhang. 2015. *ESTOMP Online User Guide*. Pacific Northwest National Laboratory, Richland, WA. [http://stomp.pnnl.gov/estomp\\_guide/eSTOMP\\_guide.stm](http://stomp.pnnl.gov/estomp_guide/eSTOMP_guide.stm).
- Fayer MJ and TB Walters. 1995. *Estimated Recharge Rates at the Hanford Site*. PNL-10285, Pacific Northwest Laboratory, Richland, WA.
- Fecht KR, SP Reidel, and AM Tallman. 1985. *Paleodrainage of the Columbia River System on the Columbia Plateau of Washington State - A Summary*. RHO-BW-SA-318-P, Rockwell International Corp., Richland, WA.
- Fink JB, MT Levitt, DF Rucker, and MB Skorska. 2010. "Detection of Historical Pipeline Leak Plumes Using Non-Intrusive , Geophysical Techniques at the Hanford Nuclear Site, Washington, USA." *WM2011 Conference*, March 7-11, 2011. Phoenix, AZ.
- Fluor Hanford Inc. 2008a. *Logistics and Processing Report Airborne Magnetic and HeliGEOTEM® II Survey*. Airborne Magnetic and HeliGEOTEM Ii Survey. Job No. 08027, Richland, WA.
- Fluor Hanford Inc. 2008b. *Resolve Survey*. Report #08027R, Richland, WA.
- Fraser DC. 1978. "Resistivity Mapping with an Airborne Multicoil Electromagnetic System." *Geophysics* 43 (I): 144–72.
- Fugro Airborne Surveys. 2010. *EM Interpretation Report Airborne RESOLVE® and HeliGEOTEM® II Survey*. Job No. 10554, Ottawa, Ontario.
- Gander MJ, KD Leary, MT Levitt, CW Miller, and DF Rucker. 2011. "Geophysics and Site Characterization at the Hanford Site : The Successful Use of Electrical Resistivity to Position Boreholes to Define Deep Vadose Zone Contamination-11509." *WM2011 Conference*, March 7-11, 2011, 15.
- Geomatrix Consultants Inc. 2005. *Evaluation of Geophysical Technologies for Subsurface Characterization*. Project No. 10960, Denver, CO.
- Haldar SK. 2018. "Exploration Geophysics, Magnetic Survey." In *Mineral Exploration: Principles and Applications*, 111–13. Elsevier. <https://doi.org/10.1016/B978-0-12-814022-2.00006-X>.
- Hammond TB and D Lupton. 2015. *Development of the Hanford South Geologic Framework Model, Hanford Site, Washington*. ECF-HANFORD-13-0029, Revision 2, CH2M Hill Plateau Remediation Company, Richland, WA.
- Harari Z. 1996. "Ground-Penetrating Radar (GPR) for Imaging Stratigraphic Features and Groundwater in Sand Dunes." *Journal of Applied Geophysics* 36 (1): 43–52. [https://doi.org/10.1016/S0926-9851\(96\)00031-6](https://doi.org/10.1016/S0926-9851(96)00031-6).
- Huang H and DC Fraser. 1996. "The Differential Parameter Method for Multifrequency Airborne Resistivity Mapping." *Geophysics* 61 (1): 100–109.

- Huisman JA and SS Hubbard. 2003. “Measuring Soil Water Content with Ground Penetrating Radar A Review.” *Vadose Zone* 2 (4): 476–91. <https://doi.org/10.2113/2.4.476>.
- Hyde ER, MA Speece, CA Link, TR Repasky, MD Thompson, and SF Miller. 2011. “A Seismic Landstreamer Survey at the Hanford Site, Washington, U.S.A.” *Environmental and Engineering Geoscience* 17 (3): 227–39. <https://doi.org/10.2113/gsegeosci.17.3.227>.
- Isono T. 1984. “Density, Viscosity, and Electrolytic Conductivity of Concentrated Aqueous Electrolyte Solutions at Several Temperatures. Alkaline-Earth Chlorides, LaCl<sub>3</sub>, Na<sub>2</sub>SO<sub>4</sub>, NaNC<sub>3</sub>, NaBr, KNC<sub>3</sub>, KBr, and Cd(NO<sub>3</sub>)<sub>2</sub>.” *Journal of Chemical and Engineering Data* 29 (1): 45–52. <https://doi.org/10.1021/je00035a016>.
- Johnson TC, LD Slater, D Ntarlagiannis, FD Day-Lewis, and M Elwaseif. 2012. “Monitoring Groundwater-Surface Water Interaction Using Time-Series and Time-Frequency Analysis of Transient Three-Dimensional Electrical Resistivity Changes.” *Water Resources Research* 48 (7).
- Johnson TC and D Wellman. 2015. “Accurate Modelling and Inversion of Electrical Resistivity Data in the Presence of Metallic Infrastructure with Known Location and Dimension.” *Geophysical Journal International* 202 (2): 1096–1108. <https://doi.org/10.1093/gji/ggv206>.
- Johnson TC. 2014. *E4D: A Distributed Memory Parallel Electrical Geophysical Modeling and Inversion Code User Guide - Version 1.0*. PNNL-SA-23783, Pacific Northwest National Laboratory, Richland, WA.
- Johnson TC, GE Hammond, and X Chen. 2017. “PFLOTRAN-E4D: A Parallel Open Source PFLOTRAN Module for Simulating Time-Lapse Electrical Resistivity Data.” *Computers and Geosciences* 99 (September 2016): 72–80. <https://doi.org/10.1016/j.cageo.2016.09.006>.
- Johnson TC, and DM Wellman. 2013. *Re-Inversion of Surface Electrical Resistivity Tomography Data from the Hanford Site B-Complex*. PNNL-22520, Pacific Northwest National Laboratory, Richland, WA.
- Johnson TC, RJ Versteeg, A Ward, FD Day-Lewis, and ARevil. 2010. “Improved Hydrogeophysical Characterization and Monitoring through Parallel Modeling and Inversion of Time-Domain Resistivity and Induced-Polarization Data.” *Geophysics* 75 (4).
- Johnson TC, R Versteeg, J Thomle, G Hammond, X Chen, and J Zachara. 2015. “Four-Dimensional Electrical Conductivity Monitoring of Stage-Driven River Water Intrusion: Accounting for Water Table Effects Using a Transient Mesh Boundary and Conditional Inversion Constraints.” *Water Resources Research* 51: 1–20. [https://doi.org/10.1016/0022-1694\(68\)90080-2](https://doi.org/10.1016/0022-1694(68)90080-2).
- Jol HM and DG Smith. 1991. “Ground Penetrating Radar of Northern Lacustrine Deltas.” *Canadian Journal of Earth Sciences* 28 (12): 1939–47. <https://doi.org/10.1139/e91-175>.
- Kemna A, J Huisman, E Zimmerman, R Martin, Y Zhao, A Treichel, A Orozco, and T Fechner. 2014. “Broadband Electrical Impedance Tomography for Subsurface Characterization Using Improved Corrections of Electromagnetic Coupling and Spectral Regularization.” In *Tomography of the Earth's Crust: From Geophysical Sounding to Real-Time Monitoring*. Springer, Cham. [https://doi.org/10.1007/978-3-319-04205-3\\_1](https://doi.org/10.1007/978-3-319-04205-3_1).

Knight R, J Irving, E Freeman, and P Tercier. 2003. "The Use of GPR as a Means of Locating Clastic Dikes." In *Symposium on the Application of Geophysics to Engineering and Environmental Problems*, 221–27. Society of Exploration Geophysicists.

Knight RJ, JD Irving, P Tercier, and GJ Freeman. 2007. "A Comparison of the Use of Radar Images and Neutron Probe Data to Determine the Horizontal Correlation Length of Water Content." *Subsurface Hydrology: Data Integration for Properties and Processes* 171 (January): 31–44. <https://doi.org/10.1029/171GM05>.

Lanigan DC, GV Last, BN Bjornstad, PD Thorne, and WD Webber. 2010. *Hanford Site Guidelines for Preparation and Presentation of Geologic Information*. PNNL-18819, Pacific Northwest National Laboratory, Richland, WA.

Last GV and DG Horton. 2000. *Review of Geophysical Characterization Methods Used at the Hanford Site*. PNNL-13149, Pacific Northwest National Laboratory, Richland, WA.

Legault JM. 2015. "Airborne Electromagnetic Systems--State of the Art and Future Directions." *CSEG Recorder* 40 (6): 38–49.

Lesmes DP and SP Friedman. 2005. "Relationships between the Electrical and Hydrogeological Properties of Rocks and Soils." In *Hydrogeophysics*, 87–128. Springer Netherlands. [https://doi.org/10.1007/1-4020-3102-5\\_4](https://doi.org/10.1007/1-4020-3102-5_4).

Lin C, C Lin, and C Chien. 2017. "Dispersion Analysis of Surface Wave Testing – SASW vs. MASW." *Journal of Applied Geophysics* 143: 223–30. <https://doi.org/10.1016/j.jappgeo.2017.05.008>.

Lin Y. 2007. "Characterizing Vs Profiles by the SASW Method and Comparison with Other Seismic Methods." Doctoral Dissertation. The University of Texas at Austin.

MacQueen JD and E Mann. 2007. *Borehole Gravity Meter Surveys at the Waste Treatment Plant, Hanford, Washington*. PNNL-16490, Pacific Northwest National Laboratory, Richland, WA.

Mankinen EA, EE Larson, CS Gromme, M Prevot and RS Coe. 1987. "The Steens Mountain ( Oregon) Geomagnetic Polarity Transition ( USA). 3. Its Regional Significance." *Journal of Geophysical Research* 92 (B8): 8057–76. <https://doi.org/10.1029/JB092iB08p08057>.

Martin CJ. 2010. *Overview of Hanford Hydrogeology. Hanford Site Groundwater Monitoring and Performance Report: 2009*. DOE/RL-2010-11, Rev. 1, U.S. Department of Energy, Richland Operations Office, Richland, WA.

Myers DA, Rucker D, M Levitt, B Cubbage, and C Henderson. 2009. *Surface Geophysical Exploration of SX Tank Farm at the Hanford Site: Results of Background Characterization with Magnetics and Electromagnetics*. RPP-RPT-42, Hanford Site, Richland, WA.

Murray CJ and GV Last. 2005. *Review of Geophysical Techniques to Define the Spatial Distribution of Subsurface Properties or Contaminants*. PNNL-15305, Pacific Northwest National Laboratory, Richland, WA.

Nabighian MN, VJS Grauch, RO Hansen, TR LaFehr, Y Li, JW Peirce, JD Phillips and ME Ruder. 2005. "The Historical Development of the Magnetic Method in Exploration." *Geophysics* 70 (6): 33ND-61ND. <https://doi.org/10.1190/1.2133784>.

- Neal A. 2004. “Ground-Penetrating Radar and Its Use in Sedimentology: Principles, Problems and Progress.” *Earth-Science Reviews* 66 (3–4): 261–330. <https://doi.org/10.1016/j.earscirev.2004.01.004>.
- Niu Q and C Zhang. 2018. “Physical Explanation of Archie’s Porosity Exponent in Granular Materials: A Process-Based, Pore-Scale Numerical Study.” *Geophysical Research Letters* 45 (4): 1870–77. <https://doi.org/10.1002/2017GL076751>.
- NQAP-2012, *Nuclear Quality Assurance Program (NQAP) Manual*. Pacific Northwest National Laboratory, Richland, WA.
- Oostrom M, MJ Truex, ML Rockhold, and TC Johnson. 2017. “Deep Vadose Zone Contaminant Flux Evaluation at the Hanford BY-Cribs Site Using Forward and Imposed Concentration Modeling Approaches.” *Environmental Processes* 4 (4): 771–97. <https://doi.org/10.1007/s40710-017-0272-5>.
- Park CB, RD Miller, J Xia, and J Ivanov. 2007. “Multichannel Analysis of Surface Waves ( MASW ) Active and Passive Methods.” *The Leading Edge*, 26.1, 60–64.
- Pelton JR. 2012. “Near-Surface Seismology: Surface-Based Methods.” In *Near-Surface Geophysics*, 219–64. <https://doi.org/10.1190/1.9781560801719.ch8>.
- Pluhar CJ, BN Bjornstad, SP Reidel, RS Coe, and PB Nelson. 2006. “Magnetostratigraphic Evidence from the Cold Creek Bar for Onset of Ice-Age Cataclysmic Floods in Eastern Washington during the Early Pleistocene.” *Quaternary Research* 65 (1): 123–35. <https://doi.org/10.1016/j.yqres.2005.06.011>.
- Rabbel W. 2010. “Seismic Methods.” In *Groundwater Geophysics: A Tool for Hydrogeology*, 23–84. Berlin: Springer. <https://doi.org/10.1007/978-3-540-88405-7>.
- Reidel SP and TL Tolan. 2013. “The late Cenozoic evolution of the Columbia River system in the Columbia River flood basalt province.” *Geological Society of America Special Papers*, 497:201-230.
- Reynolds JH. 2002. “Magnetostratigraphy Adds a Temporal Dimension to Basin Analysis: Search and Discovery Article-Online Article.”
- Richard BH, JT Lillie, and RA Deju. 1977. *Gravity Studies of the Hanford Reservation, Richland, Washington*. RHO-BWI-C—4, Atomic International Division, Richland, WA.
- Robinson J, L Slater, T Johnson, A Shapiro, C Tiedeman, D Ntarlagiannis, C Johnson, et al. 2015. “Imaging Pathways in Fractured Rock Using Three-Dimensional Electrical Resistivity Tomography.” *Groundwater* 54 (2): 1–16. <https://doi.org/10.1111/gwat.12356>.
- Robinson J, T Johnson, and M Rockhold. 2019. “Feasibility Assessment of Long-term Electrical Resistivity Monitoring of a Nitrate Plume.” *Groundwater*, April, gwat.12899. <https://doi.org/10.1111/gwat.12899>.
- Rockhold ML, FA Spane, TW Wietsma, DR Newcomer, RE Clayton, I Demirkanli, DL Saunders, MJ Truex, MM Valenta-Snyder, and CJ Thompson. 2018. *Physical and Hydraulic Properties of Sediments from the 200-DV-1 Operable Unit*. PNNL-27846, RPT-DVZ-CHPRC 0005, Rev. 0, Pacific Northwest National Laboratory, Richland, WA.

- Routh PS and DW Oldenburg. 2001. "Electromagnetic Coupling in Frequency-Domain Induced Polarization Data: A Method for Removal." *Geophysical Journal International* 145 (1): 59–76. <https://doi.org/10.1111/j.1365-246X.2001.00384.x>.
- Rucker D, M Levitt, and B Cabbage. 2007. *Surface Geophysical Exploration of B, BX, and BY Tank Farms at the Hanford Site: Results of Background Characterization with Magnetics and Electromagnetics*. Vol. RPP-RPT-34, hydroGEOPHYSICS, Inc., Richland, WA.
- Schuck A and G Lange. 2007. "Seismic Methods." *Environmental Geology*, Springer, Berlin, Heidelberg, 337–402.
- Singha K, F Day-Lewis, T Johnson, and L Slater. 2014. "Advances in Interpretation of Subsurface Processes with Time-Lapse Electrical Imaging." *Hydrological Processes*. <https://doi.org/10.1002/hyp.10280>.
- Slater LD, D Ntarlagiannis, FD Day-Lewis, K Mwakanyamale, RJ Versteeg, A Ward, C Strickland, CD Johnson, and JW Lane. 2010. "Use of Electrical Imaging and Distributed Temperature Sensing Methods to Characterize Surface Water–Groundwater Exchange Regulating Uranium Transport at the Hanford 300 Area, Washington." *Water Resources Research* 46 (10): 1–13. <https://doi.org/10.1029/2010WR009110>.
- Smith DG and HM Jol. 1995. "Ground Penetrating Radar: Antenna Frequencies and Maximum Probable Depths of Penetration in Quaternary Sediments." *Journal of Applied Geophysics* 33 (1–3): 93–100. <https://doi.org/10.1358/dof.2006.031.12.1045051>.
- Spain E and A Venkatanarayanan. 2014. "Review of Physical Principles of Sensing and Types of Sensing Materials." *Comprehensive Materials Processing*. Vol. 13. Elsevier. <https://doi.org/10.1016/B978-0-08-096532-1.01302-9>.
- Spies BR. 1989. "Depth of Investigation in Electromagnetic Sounding Methods" *Geophysics* 54 (7): 872–88.
- Steeple DW. 2005. "Shallow Seismic Methods." In *Hydrogeophysics*, 215–51. Dordrecht: Springer Netherlands. [https://doi.org/10.1007/1-4020-3102-5\\_8](https://doi.org/10.1007/1-4020-3102-5_8).
- Stokoe K, Y Lin, S Hwang, and J Roberts. 2014. *Hanford Site-Wide Probabilistic Seismic Hazard Analysis (PSHA): Seismic Shear Wave Velocity Profiling at Hanford, WA*. PNNL-23361, Pacific Northwest National Laboratory, Richland, WA.
- Strickland, CE, MJ Truex, RD Mackley, and TC Johnson. 2018. *Deep Vadose Zone Monitoring Strategy for the Hanford Central Plateau*. PNNL-28031, Pacific Northwest National Laboratory, Richland, WA.
- Topp C. 1980. "Electromagnetic Determination of Soil Water Content:" *Water Resources Research* 16 (3): 574–82.
- Vanderborght J, A Kemna, H Hardelauf, and H Vereecken. 2005. "Potential of Electrical Resistivity Tomography to Infer Aquifer Transport Characteristics from Tracer Studies: A Synthetic Case Study." *Water Resources Research* 41 (6): 1–23. <https://doi.org/10.1029/2004WR003774>.
- Veeken PCH and M Da Silva. 2004. "Seismic Inversion Methods and Some of Their Constraints." *First Break* 22 (6): 47–70.

Vereecken H, J Huisman, H Bogena, J Vanderborght, J Vrugt, and JW Hopmans. 2008. "On the Value of Soil Moisture Measurements in Vadose Zone Hydrology: A Review." *Water Resources Research* 44 (4). <https://doi.org/10.1029/2008WR006829>.

Wallin EL, TC Johnson, WJ Greenwood, and JM Zachara. 2013. "Imaging High Stage River-Water Intrusion into a Contaminated Aquifer along a Major River Corridor Using 2-D Time-Lapse Surface Electrical Resistivity Tomography." *Water Resources Research* 49 (3): 1693–1708. <https://doi.org/10.1002/wrcr.20119>.

Ward SH. 1988. "The Resistivity and Induced Polarization Methods." *Symposium on the Application of Geophysics to Engineering and Environmental Problems*, 147–89. <http://www.earthdoc.org/publication/publicationdetails/?publication=47435>.

White MD and M Oostrom. 2006. *STOMP Subsurface Transport Over Multiple Phases, Version 4: User's Guide*. PNNL-15782 (UC-2010), Pacific Northwest National Laboratory, Richland, WA. <https://stomp.pnl.gov>.

Williams BA, BN Bjornstad, R Schalla, and MD Webber. 2002. *Revised Hydrogeology for the Suprabasalt Aquifer System, 200-West Area and Vicinity, Hanford Site, Washington*. PNNL-13858, Pacific Northwest National Laboratory, Richland, WA.

Williams BA, BN Bjornstad, R Schalla, and WD Webber. 2000. *Revised Hydrogeology for the Suprabasalt Aquifer System, 200-East Area and Vicinity, Hanford Site, Washington*. PNNL-12261, Pacific Northwest National Laboratory, Richland, WA.

Wynn JC. 1974. "Electromagnetic Coupling in Induced Polarization." Doctoral Dissertation. The University of Arizona.

Yaede JR, JH McBride, ST Nelson, CB Park, JA Flores, SJ Turnbull, DG Tingey, et al. 2015. "A Geophysical Strategy for Measuring the Thickness of the Critical Zone Developed over Basalt Lavas." *Geosphere* 11.2, 514–32. <https://doi.org/10.1130/GES01142.1>.

Yue WZ. 2019. "Pore-scale Explanation of the Archie's Cementation Exponent: Microstructure, Electrical Anisotropy and Numerical Experiments." *Geophysical Research Letters* 46: 9. <https://doi.org/10.1029/2019GL082585>.

Zhao Y, E Zimmermann, E Zimmermann, and A Kemna. 2015. "Phase Correction of Electromagnetic Coupling Effects in Cross-Borehole EIT Measurements." *Measurement Science and Technology PAPER* 26. <https://doi.org/10.1088/0957-0233/26/1/015801>.

Zhu Y, TC Johnson, J Thomle, C Strickland, X Song, and JC Stegen. "Joint Hydrogeophysical Inversion for Monitoring Dynamic Mass Flux at the Groundwater-Surface Water Interface." *Water Resources Research*, Submitted.

## Appendix A

# Proposed Activities Needed to Support the ERT Field Survey Evaluation

### A.1 Introduction

The groundwater flow and transport numerical simulations documented in this report were based on the established Hanford Site geologic framework model (Ch2MHill 2016), but inherently include uncertainty due to the sparsity of data within this region. Simulated movement of an injected tracer under ambient groundwater flow conditions depends on key input parameters such as the hydraulic conductivity and porosity of the aquifer material, hydraulic gradient, and groundwater flow directions. Likewise, electrical resistivity tomography (ERT) measurements are affected by data noise levels that vary from site to site and can impact the ability to image deep stratigraphic targets effectively. Collection of site-specific measurements that reduce these uncertainties will further inform the evaluation of the use of ERT and tracer injection for stratigraphic identification.

Field tests will consist of a limited ERT campaign between 200 East and West. Additional data analyses will include a review of available pump-and-treat (P&T) flow and water-level data. Numerical simulations of observed aquifer and well responses to changes in pumping rates (e.g., shutdown and restart events) will be analyzed using inverse groundwater modeling to estimate hydraulic conductivity and porosity. Finally, the data from these field and numerical simulation tests will be used to perform an ERT sensitivity analysis on the volume and concentration of injected tracer for large-scale ERT imaging.

This appendix is intended to provide a general overview and summary of proposed activities with a multi-phased approach for obtaining site-specific ERT data and aquifer hydraulic properties. Details on the test design, sampling, and analyses methodology will be described in forthcoming work plans.

### A.2 Site-Specific 2D ERT Data collection

Surface ERT measurements will be collected along a 2.3-km-long transect running east-to-west near existing P&T injection well 699-46-68 (Figure A.1). The primary objectives for this field activity are to observe the amount of ERT data noise at this site and evaluate the ERT imaging depth resolution. Thirty-two electrodes will be spaced every 80 m and consist of 10-in. (25 cm) long steel stakes driven into the ground. Electrical control boxes will enclose the electrodes and provide a protection boundary (Figure A.2). If needed, heavy-duty “yellow jacket” cable protectors will be used for ERT cable road crossings. A mobile trailer will be temporarily parked on site to enclose the ERT data acquisition and processing equipment.

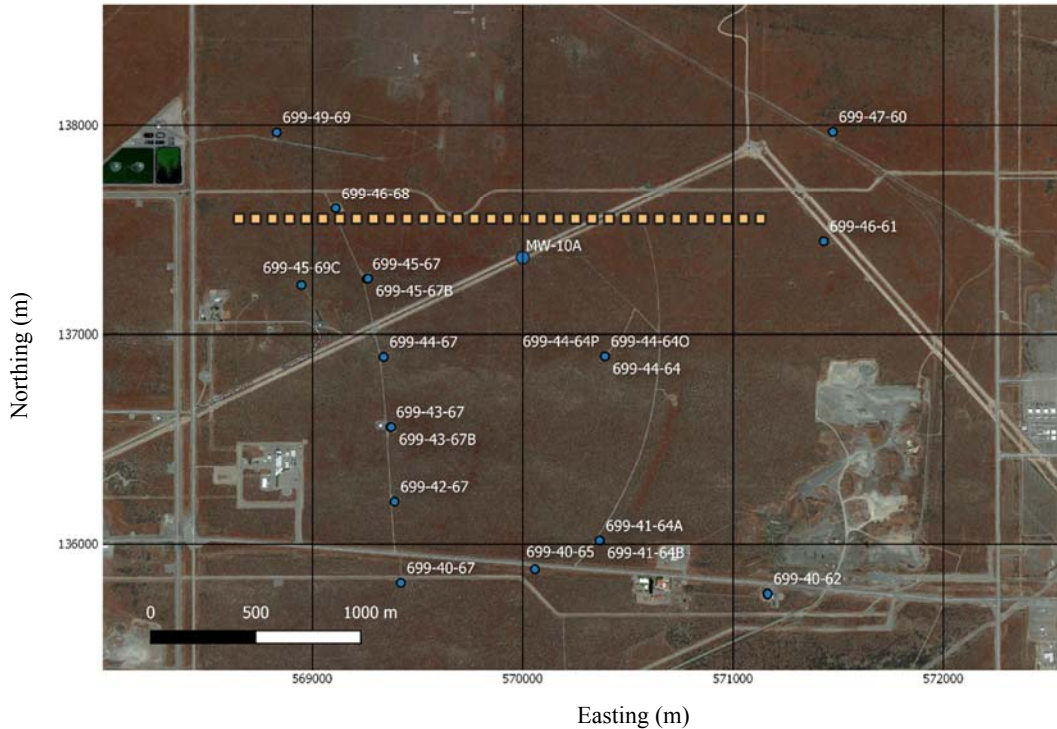


Figure A.1. Map showing the proposed ERT transect within the 200-ZP-1 operable unit. Electrodes locations are shown as yellow squares. Existing wells are shown as blue circles with the exception of MW-10A, which is a proposed well used in the ERT evaluation (Section 5).

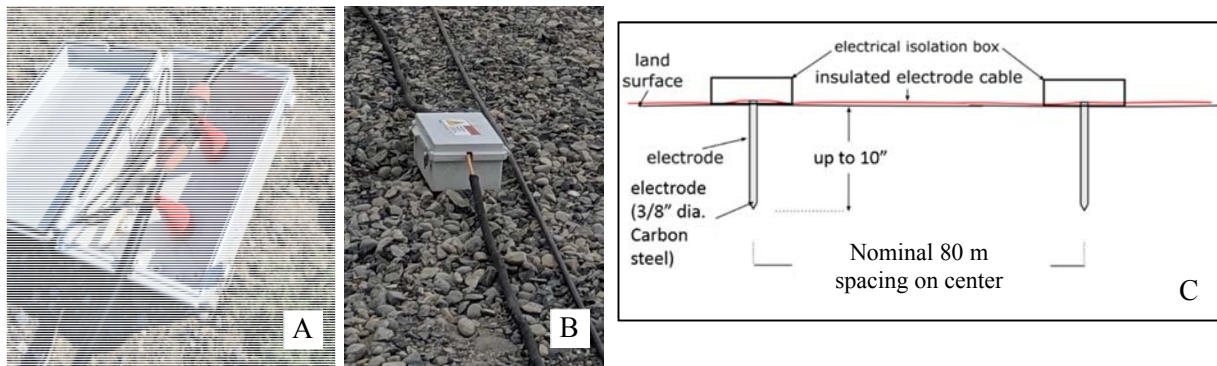


Figure A.2. Photo images showing examples of ERT electrode installations. Electrical control boxes are shown with lid open (A) and closed (B). A generalized schematic with the electrode spacing, diameter, and installation depth is shown in (C).

### A.3 Numerical Modeling of Site-specific Hydraulic Properties

Hydraulic conductivity and porosity are two important parameters that directly influence the transport behavior (velocity and direction) of an emplaced groundwater tracer. When changes in P&T extraction and injection flow rates occur, they impose a hydraulic stress on the aquifer. These imposed aquifer stresses are manifest as observable pressure responses in wells screened within the aquifer. For example, when a P&T injection well is turned off (e.g., for maintenance), water levels in that well and adjacent

wells decrease in response. The character of these pressure response are in part, controlled by bulk aquifer hydraulic properties. Historical pressure and flow rate data from P&T wells are recorded by the supervisory control and data acquisition (SCADA) system. If a sufficient number of these events have occurred and flow and pressure data are available in sufficient quality and quantity, then it is possible that these imposed stress events can be used to estimate hydraulic conductivity and porosity using an inverse groundwater flow model. This approach utilizes shutdown-restart or flow-rate change events that have already occurred (opportunistic events) in any number of P&T wells within the study area. The obvious benefit of this approach is that these shutdown-restart cycles have already occurred, and evaluation of the opportunistic aquifer stress events requires no additional operational changes, costs, or downtime in the system.

It may also be necessary or desirable to design intentional P&T well shutdown-restart events in select wells and sequences to either supplement the opportunistic events or create more controlled stress-response signals. For example, the unconfined aquifer P&T injection wells shown within the dashed red polygon in Figure A.3 could be cycled on and off in a coordinated sequence to create multiple aquifer stress tests. The sequence would consist of the following:

- All the wells within the test area shown in Figure A.3 are shut down and water levels are allowed to recover to static
- A single P&T injection well would be restarted, allowed to run at a constant-injection rate for a specified period of time, and then shut down.
  - Other nearby P&T wells would be shut down during this time and would be used as observation wells for aquifer pressure response
- This would be repeated for other P&T wells in the test area.

Coordinated P&T shutdown events with pressure monitoring in nearby wells would create a rich dataset in which reciprocal stress-observation responses could be inversely modeled for hydraulic conductivity and porosity. Shutdown events need to be designed to minimize operational downtime since these injection wells are used for flow-path control for the 200-ZP-1 operable unit carbon tetrachloride plume.



## A.5 References

Ch2MHill. 2016. *Development of the Hanford South Geologic Framework Model, Hanford Site , Washington Fiscal Year 2016 Update*. ECF-HANFORD-13-0029 Rev. 4, CH2M Hill Plateau Remediation Company, Richland, WA.

DOE. 2018. *Calendar Year 2017 Annual Summary Report for Pump-and-Treat Operations in the Hanford Central Plateau Operable Units*. DOE/RL-2017-68, Rev. 0, U.S. Department of Energy, Richland Operations Office, Richland, WA.

# **Pacific Northwest National Laboratory**

902 Battelle Boulevard  
P.O. Box 999  
Richland, WA 99354  
1-888-375-PNNL (7665)

***[www.pnnl.gov](http://www.pnnl.gov)***